RESEARCH ARTICLE

Geochemical, isotopic and single crystal ^{40}Ar/^{39}Ar age constraints on the evolution of the Cerro Galán ignimbrites

**Suzanne Mahlburg Kay · Beatriz Coira ·
Gerhard Wörner · Robert W. Kay · Bradley S. Singer**

Abstract The giant ignimbrites that erupted from the Cerro Galán caldera complex in the southern Puna of the high Andean plateau are considered to be linked to crustal and mantle melting as a consequence of delamination of gravitationally unstable thickened crust and mantle lithosphere over a steepening subduction zone. Major and trace element analyses of Cerro Galán ignimbrites (68–71% SiO$_2$) that include 75 new analyses can be interpreted as reflecting evolution at three crustal levels. AFC modeling and new fractionation corrected δ^{18}O values from quartz (+7.63–8.85‰) are consistent with the ignimbrite magmas being near 50:50 mixtures of enriched mantle (^{87}Sr/^{86}Sr~ 0.7055) and crustal melts (^{87}Sr/^{86}Sr near 0.715–0.735).

S. M. Kay (✉) · R. W. Kay
Department of Earth and Atmospheric Sciences, Cornell University,
Snee Hall,
Ithaca, NY 14853, USA
e-mail: smk16@cornell.edu

B. Coira
CONICET,
Casilla de Correo 258,
4600 S.S. de Jujuy, Argentina

G. Wörner
Abt. Geochemie, GZG, Universität Göttingen,
Göttingen 37077, Germany

B. S. Singer
Department of Geology Geophysics, University of Wisconsin,
Madison, WI 53706, USA

Processes at lower crustal levels are predicated on steep heavy REE patterns (Sm/Yb=4–7), high Sr contents (>250 ppm) and very low Nb/Ta (9-5) ratios, which are attributed to amphibolite partial melts mixing with fractionating mantle basalts to produce hybrid melts that rise leaving a gravitationally unstable garnet-bearing residue. Processes at mid crustal levels create large negative Eu anomalies (Eu/Eu*=0.45–0.70) and variable trace element enrichment in a crystallizing mush zone with a temperature near 800–850°C. The mush zone is repeatedly recharged from depth and partially evacuated into upper crustal magma chambers at times of regional contraction. Crystallinity differences in the ignimbrites are attributed to biotite, zoned plagioclase and other antecrysts entering higher level chambers where variable amounts of near-eutectic crystallization occurs at temperatures as low as 680°C just preceding eruption. ^{40}Ar/^{39}Ar single crystal sanidine weighted mean plateau and isochron ages combined with trace element patterns show that the Galán ignimbrite erupted in more than one batch including a~2.13 Ma intracaldera flow and outflows to the west and north at near 2.09 and 2.06 Ma. Episodic delamination of gravitationally unstable lower crust and mantle lithosphere and injection of basaltic magmas, whose changing chemistry reflects their evolution over a steepening subduction zone, could trigger the eruptions of the Cerro Galán ignimbrites.

Introduction

The erupted units of the Cerro Galán complex include the largest Neogene ignimbrites in the southern Puna of the Andean Puna-Altiplano plateau. These ignimbrites were

extensively studied in the 1980s leading to two classic summary papers. The first by Sparks et al. (1985) presented the physical and temporal framework, and the second by Francis et al. (1989), the mineralogical, petrological and geochemical picture. Folkes et al. (2010, this volume) reappraise the physical and temporal framework of the caldera based on new geochronological and field work. This paper reexamines the geochemical framework in which the ignimbrite erupted based on new major and trace element whole rock, quartz $\delta^{18}O$ analyses, single crystal sanidine and biotite $^{40}Ar/^{39}Ar$ ages and the magmatic, tectonic and geophysical framework of the region.

On a large scale, the Cerro Galán ignimbrites are argued to be the product of melting associated with the latest Miocene to Pliocene foundering (delamination) of gravitationally unstable lower crust and lithospheric mantle over a steepening subduction zone (e.g., Kay et al. 1994, 1999; Kay and Coira 2009). This paper explores the nature and relative proportions of mantle and crustal components in the ignimbrite magmas and the depths and temperatures at which they evolved. New and existing major and trace element data are used to support a model of evolution of the ignimbrites at three crustal levels, and new quartz $\delta^{18}O$ measurements along with Sr AFC models are used to argue that the ignimbrites could be near 50/50 mixtures of enriched mantle-derived basaltic and crustal melts. Single crystal $^{40}Ar/^{39}Ar$ sanidine, systematically older $^{40}Ar/^{39}Ar$ biotite ages and variable trace element chemistry are used to show that the most recent Galán ignimbrite erupted in more than one event between at least 2.13 and 2.06 Ma.

Setting, stratigraphy, age and petrography of the Cerro Galán ignimbrites

The Miocene to Recent structural and tectonic setting of the Cerro Galán region, which is underlain by late Precambrian and Paleozoic crystalline and sedimentary rocks, has been recently summarized by Kay et al. (2008b) and Kay and Coira (2009). Miocene volcanism began in the region at about 14 Ma with large long-lived stratovolcanoes that erupted until about 6.6 Ma, when a more bimodal mafic and silicic volcanic pattern began (see Kay et al. 1999; Risse et al. 2008) that includes the Cerro Galán eruptions. The stratigraphy, petrography and volcanological features of the Cerro Galán ignimbrite complex are discussed by Sparks et al. (1985); Francis et al. (1989); Folkes et al. (2010) and others in this volume. A generalized map of the mafic and silicic flows showing the samples discussed in this paper is in Fig. 1.

The Cerro Galán ignimbrites can be divided into the older Toconquis and the younger Galán groups. Based on K/Ar biotite ages in Sparks et al. (1985) and new $^{40}Ar/^{39}Ar$

biotite ages, Folkes et al. (2010) divided the Toconquis group into the 6.4-5.5 Ma Blanco/Merihuaca, 4.8 Ma Pitas, 4.7 Ma Real Grande, 4.5 Ma Vega, and 3.8 Ma Cueva Negra ignimbrites and assigned the Galán ignimbrites ages from 2.8 to 2 Ma. As pointed out by Sparks et al. (1985) and Francis et al. (1989), the Toconquis group ignimbrites differ from the Galán group ignimbrites in being more pumice- and less-crystal rich. Modal data from thin sections of these ignimbrites as summarized from Table 1 in Francis et al. (1989) are as follows. The Toconquis pumices and whole rock ignimbrites consist of 78–90% matrix with plagioclase and biotite, smaller amounts of quartz and Fe-Ti oxides and little to no sanidine. The Real Grande and Cueva Negra ignimbrites can also contain minor amounts of hornblende and orthopyroxene. In contrast, the Galán ignimbrites are pumice-poor and crystal-rich with the outflow facies reported to average 51% matrix, 11% quartz, 18% plagioclase, 6% sanidine and 7% biotite, and the intracaldera deposits 58% matrix, 9% quartz, 17% plagioclase, 8% sanidine, and 7% biotite. The pumices in the Galán ignimbrites can have 35 to 40% phenocrysts. The Galán ignimbrites also contain titanomagnetite and trace amounts of zircon, apatite and allanite.

Sanidine and biotite $^{40}Ar/^{39}Ar$ ages in the Galán ignimbrite

As Sparks et al. (1985) were concerned that the biotite K/Ar ages that they obtained might not accurately reflect the times of eruptions of the Cerro Galán ignimbrites, they also reported Rb/Sr isochron ages of 2.39±0.15 Ma for an intracaldera tuff from a unit with a K/Ar biotite age of 3.65±0.45 Ma; of 2.03±0.07 Ma for a pumice from a Galán ignimbrite east of the caldera rim with a K/Ar biotite age of 2.57±0.16 Ma, and of 4.00±0.22 Ma for a dacite related to the Real Grande ignimbrite with a K/Ar biotite age of 4.86±0.19 Ma. To further investigate this problem, large (>mm) hand-picked crystals of sanidine and biotite from both pumice and whole-rock samples from three localities of the Galán ignimbrite have been incrementally heated using a 25 W CO_2 laser at the University of Wisconsin-Madison Rare Gas Geochronology Laboratory to generate $^{40}Ar/^{39}Ar$ age spectra. Individual age spectra were acquired from aliquots of one, two, or three crystals from each sample. Plateau ages from two or three separate incremental heating experiments were pooled to calculate weighted mean apparent and isochron ages for each sample. These ages, which were calculated using the decay constants of Steiger and Jäger (1977) with J-values relative to 28.34 Ma Taylor Creek rhyolite sanidine (Renne et al. 1998), are reported with 2σ analytical uncertainties in Table 1. Complete analytical data are in Electronic Appendix Tables A1 and A2. In addition, calculated weighted mean apparent ages and isochron ages from
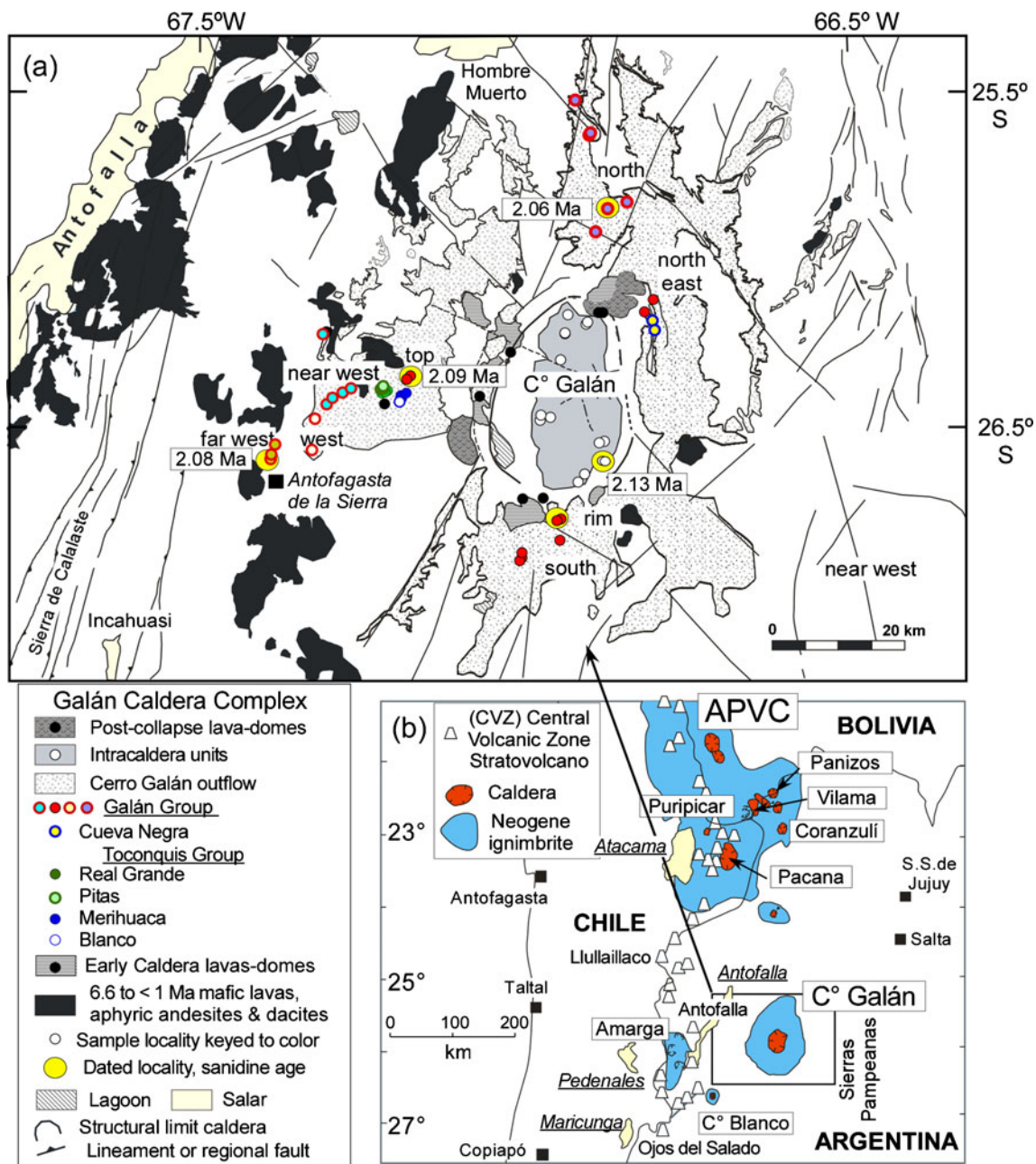
Fig. 1 **a** Generalized map of the Cerro Galán Caldera complex region showing dated localities (yellow circles) with $^{40}Ar/^{39}Ar$ sanidine ages from Table 1, localities of samples analyzed in this study coded as in legend, regions of the Cerro Galán complex referred to in text, distribution of mafic to dacitic lavas with ages overlapping the Galán ignimbrites and principle faults. Coordinates of analyzed samples are in Tables 2 and 3 and Electronic Appendix Table A4. **b** Map of a portion of the Central Andes showing the Cerro Galán ignimbrite complex relative to the Altiplano Puna Volcanic Complex (APVC) and other major plateau ignimbrite, volcanic centers, principal salars (underlined italics) and reference cities (squares). Map is modified from Kay and Coira (2009)

single crystal laser fusion measurements of biotite and sanidine on samples from two other localities are reported in Table 1 with complete analytical results in Electronic Appendix Table A3. Overall, the data from each individual locality show that most gas fractions give concordant ages, that the mean apparent (plateau) and isochron ages are in excellent agreement for the same mineral, that there is no

evidence in the isochron regressions for excess argon and that the biotite ages are always older than the sanidine age at the same locality (Table 1; Fig. 2).

The dated localities and average sanidine $^{40}Ar/^{39}Ar$ ages from this study are shown on the map in Fig. 1. The 2.13 Ma age shown in the intracaldera region at 26° 02'52.0"S, 66°53'23.3"W is from a pumice-rich tuff

Table 1 Summary of $^{40}Ar/^{39}Ar$ laser incremental heating experiments: single and multi-crystal from Galan ignimbrites

Sample	Experiment	K/Ca total	# of crystals	Total fusion Age a (Ma) ±2σ	Increments power (W)	Age Spectrum $^{39}Ar\%$	MSWD	Age a (Ma) ±2σ	N^c	Isochron Analysis $^{40}Ar/^{36}Ar_i$ ±2σ	MSWD	Age a (Ma) ±2σ
Sanidine												
SAF367a	Northern outflow (pumice-rich whole rock)											
	UW58A1b	65.9	1	2.07±0.03	0.65–5.00	100.0	0.35	2.067± 0.028	8 of 8	295.9±3.1	0.39	2.066± 0.029
	UW58A1c	76.0	2	2.05±0.03	0.65–5.00	100.0	0.35	2.048± 0.028	8 of 8	318.6± 47.2	0.22	2.043± 0.031
	weighted mean plateau age		0.92	**2.058±0.020**	weighted mean isochron age		1.17	2.060± 0.021				
SAF367b	Northern outflow (pumice-rich whole rock)											
	UW58A6a	73.4	1	2.06±0.04	0.65–3.25	100.0	0.70	2.036± 0.031	7 of 7	307.1± 15.1	0.34	2.029± 0.033
	UW58A6b	47.7	2	2.11±0.03	1.00–5.00	96.0	1.06	2.069± 0.026	7 of 8	302.9±8.2	0.59	2.057± 0.029
	UW58A6c	68.9	2	2.07±0.03	1.00–5.00	89.3	0.47	2.058± 0.025	7 of 8	264.3± 138.1	0.53	2.068± 0.047
	weighted mean plateau age		1.30	**2.056±0.016**	weighted mean isochron age		1.20	2.049± 0.020				
Combined SAF367a and SAF367b	weighted mean plateau age			**2.057±0.012**								
SAF332a	Western outflow (whole rock)											
	UW58B1a	39.9	1	2.12±0.04	0.65–5.00	100.0	1.53	2.144± 0.034	8 of 8	290.4± 19.6	1.71	2.148± 0.038
	UW58B1b	40.1	2	2.08±0.03	0.75–5.00	100.0	0.24	2.079± 0.026	8 of 8	298.4± 16.8	0.26	2.078± 0.026
	UW58B1c	64.3	2	2.09±0.03	0.75–5.00	100.0	0.42	2.085± 0.026	9 of 9	299.5± 12.7	0.42	2.085± 0.026
	weighted mean plateau age		5.20		**2.096±0.016**	weighted mean isochron age	5.00	2.094± 0.017				
SAF332b	Western outflow (pumice)											
	UW58A5a	71.9	1	2.15±0.05	1.00–2.00	95.1	0.99	2.067± 0.035	4 of 8	310.5± 364.7	1.49	2.061± 0.113
	UW58A5b	64.8	3	2.10±0.03	0.80–5.00	99.0	0.33	2.075± 0.028	7 of 8	302.9± 26.4	0.33	2.072± 0.031
	UW58A5c	68.6	1	2.13±0.03	0.93–5.00	99.1	1.91	2.095± 0.023	6 of 8	361.9± 57.3	0.37	2.084± 0.028
	weighted mean plateau age		1.13		**2.083±0.016**	weighted mean isochron age	0.21	2.078± 0.020				
SAF350p	Intracaldera tuff (pumice)											
	UW58A3a	80.6	1	2.20±0.07	0.65–2.50	98.8	1.05	2.149± 0.053	6 of 7	327.5± 70.9	1.06	2.123± 0.071

Sample	Description			Plateau age	Steps	%39Ar	MSWD	Isochron age	n	40Ar/36Ar	MSWD	Total fusion age
UW58A3b		77.8	2	2.17±0.03	0.93–5.00	96.6	2.02	2.123±0.027	6 of 8	301.4±12.0	2.02	2.122±0.029
UW58A3c		34.8	2	2.18±0.03	1.05–5.00	95.1	0.98	2.124±0.024	5 of 8	287.3±12.8	0.93	2.140±0.037
		weighted mean plateau age	0.42	**2.126±0.017**	weighted mean isochron age		0.31	2.128±0.022				
SAF339af[a]	Far western outflow (whole rock)											
UW78C33		53.2	1	2.08±0.01	7.0 (fusion)	100.0	0.58	**2.080±0.009**	10 of 10	304.2±19.5	0.56	2.074±0.017
Biotite												
SAF367a	Northern outflow (whole rock)											
UW58B4a		42.5	1	2.56±0.10	1.30–4.00	96.6	0.92	2.456±0.076	4 of 7	282.6±116.9	1.35	2.496±0.337
UW58B4b		10.1	2	2.46±0.06	1.00–3.75	98.9	1.03	2.456±0.051	7 of 8	296.3±4.3	1.20	2.453±0.057
UW58B4c		28.6	1	2.51±0.12	0.75–5.00	100.0	0.52	2.513±0.089	9 of 9	294.6±12.4	0.59	2.518±0.104
		weighted mean plateau age	0.67	**2.467±0.038**	weighted mean isochron age		0.61	2.469±0.049				
SAF367b	Northern outflow (whole rock)											
UW58B3a		5.7	1	2.43±0.08	1.00–5.00	100.0	0.26	2.444±0.062	6 of 6	280.9±33.8	0.15	2.495±0.133
UW58B3b		8.4	3	2.47±0.08	0.75–5.00	100.0	1.10	2.457±0.068	9 of 9	297.3±11.5	1.25	2.452±0.082
		weighted mean plateau age	0.08	**2.450±0.046**	weighted mean isochron age		0.30	2.464±0.070				
SAF332a	Western outflow (whole rock)											
UW58B2a		7.5	1	2.22±0.12	2.00–5.00	95.2	0.01	2.270±0.068	3 of 4	294.9±13.8	0.02	2.273±0.092
UW58B2b		19.8	3	2.35±0.05	1.63–4.00	99.0	0.91	2.336±0.043	6 of 8	276.0±26.6	0.67	2.408±0.107
		weighted mean plateau age	2.70	**2.317±0.036**	weighted mean isochron age		3.70	2.330±0.070				
SAF332b	Western outflow (pumice)											
UW58B5a		7.8	1	2.20±0.09	1.00–2.00	61.4	0.01	2.380±0.096	3 of 6	294.1±20.6	0.00	2.406±0.390
UW58B5b		19.1	3	2.35±0.10	0.75–3.75	96.8	0.25	2.378±0.077	8 of 9	294.5±16.3	0.28	2.387±0.162
		weighted mean plateau age	0.00	**2.379±0.060**	weighted mean isochron age		0.01	2.390±0.150				
SAF350p	Intracaldera tuff (pumice)											
UW58B7a		16.7	1	2.52±0.13	0.75–3.75	86.9	1.19	2.693±0.088	7 of 8	286.6±16.5	1.13	2.829±0.259
UW58B7b		16.4	1	2.66±0.18	0.63–3.75	100.0	0.26	2.678±0.146	8 of 8	293.0±7.2	0.22	2.723±0.200

Table 1 (continued)

Sample	Experiment	K/Ca	# of crystals	Total fusion Agea (Ma) ±2σ	Increments power (W)	Age Spectrum			Nc	Isochron Analysis		
						39Ar%	Agea (Ma) ±2σ	MSWD		40Ar/36Ari ±2σ	MSWD	Agea (Ma) ±2σ
	UW58B7c	40.5	1	2.65±0.13	0.65–3.75	100.0	2.667±0.117	0.28	8 of 8	292.7±7.1	0.23	2.750±0.241
SAF339af[b] Far western outflow (whole rock)				weighted mean plateau age	0.07	**2.683±0.063**	0.21	weighted mean isochron age	2.760±0.130			
	UW78D39	20.9	1	2.58±0.15	7.0 (fusion)	100.0	**2.576±0.132**	0.16	12 of 12	301.0±13.7	0.11	2.465±0.033
SAF339pa[b] Far western outflow (pumice)												
	UW78D38	13.8	1	2.59±0.10	7.0 (fusion)	100.0	**2.596±0.087**	0.11	14 of 14	299.7±8.9	0.04	2.523±0.192
SAF341[b] Southern rim (welded tuff)												
	UW78D40	17.7	1	2.39±0.10	7.0 (fusion)	100.0	**2.392±0.087**	0.17	12 of 12	313.9±46.2	0.12	2.113±0.699

[a] Calculated using decay constants of Steiger and Jäger (1977); J-value relative to 28.34 Ma Taylor Creek rhyolite sanidine (Renne et al. 1998)

[b] Laser total fusion experimints on single crystals

[c] N = number of steps or analyses included in mean age calculation

Apparent ages in bold give the best estimate for each sample

(SAF350p) in which the sanidine grains yielded 2.126± 0.017 Ma and the biotite grains yielded 2.683±0.063 Ma (Fig. 2). The biotite age is younger than, but nearly within error of the 3.04±0.15 MaK/Ar biotite age in Sparks et al. (1985) for an intracaldera flow. The 2.09 Ma age shown west of the caldera rim at 25°58.507'S, 67°12.573'W is based on sanidine ages of 2.083±0.016 Ma in a pumice (SAF332b) and of 2.096±0.016 Ma in a whole rock sample (SAF332a) from the uppermost ignimbrite at this locality. These ages are ~250 Ka younger than the respective biotite ages of 2.379±0.060 Ma and 2.317±0.036 Ma from the same samples. The 2.08 Ma age shown in the far western part of the Galán ignimbrite at 26°03'0.04"S, 67° 25'20.3"W is based on a sanidine age of 2.08±0.009 Ma from a whole rock sample (SAF399af). Biotite ages from this sample and a pumice (SAF339pa) from the same locality are~500 Ka older at 2.576 ±0.132 Ma and 2.596± 0.087 Ma respectively. The 2.06 Ma age shown on the Galán ignimbrite north of the rim at 25°39'57.9"S, 66° 52'42.2"W is based on sanidine ages of 2.058±0.020 Ma and 2.056±0.016 Ma in two whole rock samples (SAF367a and SAF367b), whose respective biotite ages of 2.467± 0.038 Ma and 2.450±0.046 Ma are~400 Ka older (Fig. 2). As the sanidine ages for these three localities are distinguishable from one another at the 95% confidence level, they are consistent with at least three eruptions over a short period of time. A biotite fusion age from a welded tuff (SAF341) without sanidine on the southern rim of the caldera at 26°0.7'34.7"S, 66°57'19.3"W yielded an age of 2.41±0.038 Ma.

A notable feature of the $^{40}Ar/^{39}Ar$ biotite and sanidine ages in Table 1 is the relatively constant difference between sanidine and biotite ages at the same locality and the differences between localities. This age spread appears to be a distinctive feature acquired in the evolution of the

individual deposits. Other studies on central Andean silicic lavas and ignimbrites have also found biotites with older ages than sanidines in the same flow (e.g., Hora et al. 2009). In North America, Charlier et al. (2007) show a 0.2–0.3 Ma age difference between sanidine and biotite ages in the large volume Fish Canyon tuff in Colorado, which they suggest is due to preservation of inherited argon in structural traps in biotite. Hora et al. (2009) have argued that biotite, whose closure temperature is higher than that of sanidine, partitions ^{40}Ar from the melt and carries a small amount of excess argon to the surface. Given the potentially complex behavior of biotite in silicic magma, the sanidine ages are considered the most accurate indicators of time since eruption in the dated deposits.

Chemical compositions of the Cerro Galán ignimbrites

New major and trace element data for 75 pumice and whole rock ignimbrite samples augment analyses in Francis et al. (1989) and elsewhere in this volume. Representative analyses are listed in Tables 2 and 3 with the complete data set in Electronic Appendix Table A4. Whole rock analyses were done by XRF and trace elements were analyzed directly on rock powders using INAA and XRF analyses, which are ideal for silicic samples as they eliminate the problems of incomplete sample dissolution of accessory minerals that can be encountered in ICP-MS analyses. Analytical techniques are discussed in Appendix 1. As indicated in Tables 2 and 3 and Electronic Appendix Table A4, both lithic-free, generally pumice-rich whole rock and pumice samples were analyzed, particularly in the Galán ignimbrites where large pumices are not common. Although scatter relative to magma compositions is introduced by whole rock analyses, comparisons of whole rock and
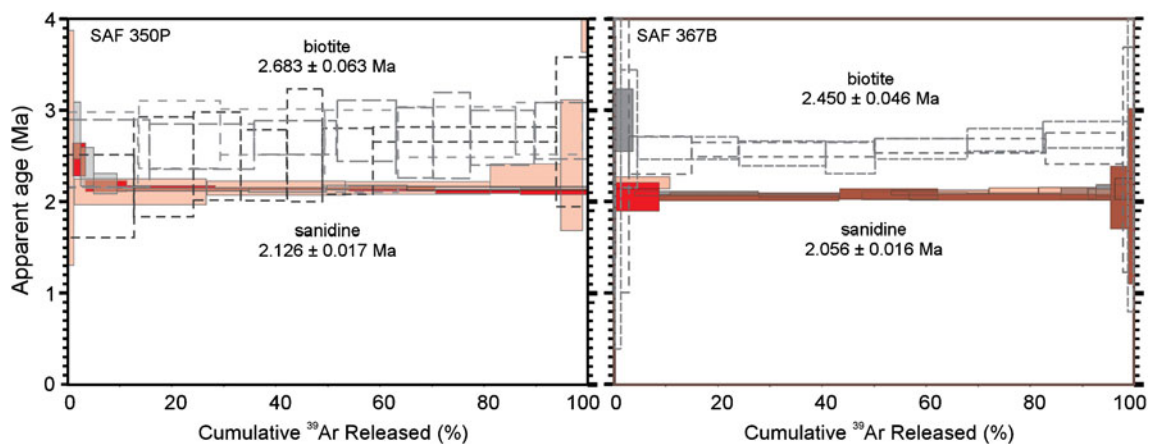

Fig. 2 $^{40}Ar/^{39}Ar$ age spectrum diagrams for sanidine and biotite in Galán ignimbrite samples SAF350p and SAF367b from Table 1. Sanidine spectra are shown as filled patterns, biotite spectra are outlined by dashed lines. The weighted mean apparent ages of each mineral are shown. In both samples, the biotite spectra give apparent ages some 400–560 ka older than the sanidine. The sanidine ages are interpreted to reflect the time since eruption, whereas the biotite ages record complex partitioning and closure to diffusion of argon during eruption

Table 2 Representative major and trace element analyses for Toconquis Group ignimbrites

Unit	Blanco	Merihuaca lower	Merihuaca middle and upper		Pitas			Real Grande			Pitas	Cueva Negra
	SAF334	SAF333p	SAF330p2	SAF330p1	SAF331a	SAF331b	SAF318bc	SAF314p	SAF315p	SAF319c	SAF320c	SAF 360
SiO$_2$	67.87	69.61	69.61	69.55	68.93	70.14	67.72	69.60	69.96	69.03	69.28	69.71
TiO$_2$	0.57	0.52	0.56	0.54	0.50	0.47	0.54	0.55	0.56	0.52	0.50	0.57
Al$_2$O$_3$	16.28	15.63	15.25	15.60	15.44	15.29	16.19	15.09	15.18	15.76	15.72	15.25
FeO	3.11	2.58	2.65	2.68	2.62	2.51	2.59	2.63	2.83	2.62	2.56	2.95
MnO	0.05	0.04	0.05	0.05	0.04	0.05	0.05	0.05	0.05	0.05	0.05	0.05
MgO	1.32	1.17	1.14	1.06	1.18	1.06	1.04	1.08	1.12	1.09	0.99	1.03
CaO	3.28	2.45	2.57	2.61	2.87	2.34	3.00	2.44	2.49	2.73	2.59	2.74
Na$_2$O	3.70	2.89	3.37	3.35	3.35	2.99	3.36	3.53	2.83	3.69	3.66	3.55
K$_2$O	3.61	4.63	4.48	4.58	4.53	4.88	4.18	4.78	4.80	4.56	4.68	3.96
P$_2$O$_5$	0.20	0.18	0.19	0.20	0.27	0.18	0.17	0.17	0.18	0.18	0.18	0.19
Total (anhydrous)	99.98	99.69	99.86	100.23	99.62	99.91	98.84	100.34	100.00	100.24	100.21	100.01
LOI	2.34	2.72	2.03	2.03	2.30	2.76	1.37	3.07	3.14	2.08	1.58	0.71
La	29.2	36.7	48.6	38.7	29.4	37.5	36.7	43.3	46.0	44.0	44.7	43.1
Ce	63.3	78.0	103.0	81.5	65.5	80.7	77.6	91.9	90.6	92.0	97.5	91.0
Nd	29.5	33.2	43.3	36.7	27.1	32.5	33.2	38.3	32.4	40.3	39.9	34.6
Sm	6.30	6.22	8.20	7.59	5.99	6.16	6.50	7.60	6.90	7.60	7.89	7.35
Eu	1.03	0.88	1.11	1.03	0.95	0.93	1.06	0.93	1.09	1.02	0.92	1.36
Tb	0.483	0.460	0.600	0.573	0.428	0.350	0.582	0.618	0.670	0.568	0.485	0.718
Yb	1.159	1.02	1.36	1.38	1.19	0.97	1.13	1.18	1.25	1.15	1.21	1.63
Lu	0.149	0.128	0.163	0.172	0.167	0.131	0.135	0.130	0.152	0.146	0.145	0.202
Y	13	10	15	14	12	10	15	13	13	13	13	18
Rb	202	237	238	237	225	237	211	261	264	286	257	190
Sr	349	285	283	302	299	286	311	271	278	274	266	310
Ba	531	638	574	582	594	692	472	533	562	489	528	486
Cs	18.5	16.6	18.5	16.7	18.0	16.2	13.6	15.5	14.4	17	15.3	30.8
U	10.3	9.0	11.2	11.0	11.0	9.2	8.5	9.9	9.3	9	9.3	11.4
Th	16.7	22.1	26.4	22.7	18.5	21.3	18.8	22.7	25.3	25	26.7	23.9
Pb		39	18	20	23	40	3					
Hf	4.9	4.8	4.9	5.4	4.6	5.1	4.6	4.4	5.0	5	5.1	5.0
Zr	162	176	174	175	153	176	176	184	189	170	171	166
Nb	13	12	14	14	14	11	13	17	17	14	13	16
Ta	1.9	1.6	2.0	1.9	1.9	1.6	1.5	1.7	1.6	1.7	1.6	2.4
Sc	6.2	5.7	5.7	5.4	5.9	5.3	5.4	4.8	5.1	5	5.1	6.5
Cr	14	18	14	11	11	15	13	13	13	18	15	9
Ni	1	2	4	10	3	5	3	3	1	11	7	4
Co	51	6	6	6	7	6	6	5	5	7	6	6

Additional REEs by ICPMS		Gd=4.90, Dy=3.28, Ho=0.56, Er=1.52, Tm=0.21					Gd=4.89, Dy=3.19, Ho=0.54, Er=1.52, Tm=0.21	Gd=4.24, Dy=2.67, Ho=0.47, Er=1.29, Tm=0.18		
Latitude °S	25.986	25.986	25.980	25.980	25.980	25.980	25.977	25.977	25.976	25.976	25.853
Longitude °W	67.214	67.214	67.219	67.219	67.219	67.219	67.228	67.228	67.235	67.235	66.817
Elevation (m)	4282	4920	4305	4350	3985	3985	4291	4291	4300	4300	4657
Notes	pumice-rich	white pumice	pink pumice	white pumice	white pumice	white pumice	white pumice	pink pumice	pumice	pumice	pumice-rich fiamme

See Electronic Appendix Table A4 for this paper for complete data set for Toconquis Group ignimbrites

Analytical methods discussed in Appendix 1

pumice samples in this study and in that of Francis et al. (1989) show that analyses can be similar to a first order and that ratios of trace elements concentrated in the glassy matrix are the least sensitive as to whether whole rock or pumice samples are analyzed (see Figs. 3, 4, 5, 6, 7 and 8). Labeling of the Galán ignimbrite analyses in Figs. 3 and 5 with respect to the regions indicated in Fig. 1 shows that analyses from the same region often cluster regardless of the sample type analyzed. Some of the largest differences within a region can be among the pumices or most pumice-rich samples.

Francis et al. (1989) described the first order major element characteristics of the Cerro Galán ignimbrites. As shown in Fig. 3, most of the ignimbrites are metaluminous to slightly peraluminous (Al/[Na+K+Ca]~0.94–1.06) rhyodacites (67–71% SiO_2 anhydrous) with 3-4% Na_2O and 4-5% K_2O. Compared to other Puna ignimbrites, the Cerro Galán ignimbrites are the most Na-rich, most like A-type granites, and among the least peraluminous (Kay et al. 2008a). Some intracaldera ignimbrites have lower Na_2O (2.5–3%) and K_2O (3.5–4%) and higher SiO_2, up to 72%) contents. FeO/MgO ratios (2.1–3) are in the calc-alkaline range on Miyashiro plots and TiO_2 contents are 0.43–0.65%. The Toconquis ignimbrites all have<0.56% TiO_2 and FeO (total Fe)/MgO ratios<2.6. Representative REE and other trace element data are shown on chondrite and mantle normalized plots in Fig. 4 and selected element variation diagrams in Figs. 5, 6 and 7. These plots and the data in Tables 2 and 3 and Electronic Appendix Table A4 show that overall REE patterns range from moderate to steep (La/Yb~20–45), heavy REE patterns are steep (Sm/Yb~4–7.5), Yb (1.1–1.9 ppm) and Y (10–21 ppm) contents are low, and negative Eu anomalies are large (Eu/Eu*= 0.40–0.70). The extended element diagram in Fig. 4 shows strong Nb and weak Ta depletions, which reflect notably low Nb/Ta ratios (6–10) that can be attributed to high Ta and low Nb contents (Fig. 7). Figure 5 shows that Ba/La (most<15), La/Ta (most 14–30) and Zr/Nb (<15) ratios generally fall in the intraplate-like range, and that Ba/Th ratios (10–33) are lower than those in either intraplate or arc rocks reflecting relatively low Ba and high Th contents. Th/U ratios are 1.8 to 4, with those in the Toconquis ignimbrites<3. The mixture of an arc-like Nb depletion and intraplate-like trace element ratios is the result of a combination of both high pressure source and low pressure differentiation processes as discussed below. xOverall, the Cerro Galán ignimbrites have lower Ba and higher Rb, Ta and Nb contents than the less voluminous silicic Neogene ignimbrites in the southern Puna (see Schnurr et al. 2007).

In detail, there are differences in trace element contents between the Toconquis and Galán ignimbrites. Francis et al. (1989) pointed to a pattern of relatively low Y and Rb contents in the Merihuaca ignimbrites, higher Sr at the

Table 3 Representative major and trace element analyses for Intracaldera and Galán Group ignimbrites

Unit	Intracaldera			Galán south	Galán north	Galán far west			Galán west	Galán top	
	SAF350p	SAF 354	SAF-308	SAF341	SAF367b	SAF 366b	SAF57	SAF339pa	SAF-338p	SAF332a	SAF332pb
SiO_2	70.52	69.15	67.88	68.34	69.81	70.34	68.02	–	69.30	66.79	70.12
TiO_2	0.63	0.62	0.64	0.61	0.57	0.61	0.69	–	0.56	0.61	0.64
Al_2O_3	14.64	16.46	15.97	15.68	15.21	14.59	14.78	–	15.49	15.42	14.46
FeO	3.22	3.32	3.35	2.88	2.94	3.08	2.82	2.52	2.80	2.84	2.98
MnO	0.05	0.04	0.04	0.05	0.05	0.05	0.04	–	0.05	0.05	0.06
MgO	1.20	1.16	1.29	1.06	1.10	1.29	1.08	–	1.19	1.41	1.31
CaO	2.37	2.34	2.66	2.50	2.55	2.53	2.35	–	2.43	3.28	2.37
Na_2O	2.81	2.94	3.36	3.75	3.43	3.26	3.47	3.12	3.20	4.16	3.26
K_2O	4.32	4.09	4.15	4.62	4.33	4.27	5.19	–	4.56	4.76	4.30
P_2O_5	0.18	0.19	0.13	0.20	0.19	0.18	0.20	–	0.18	0.20	0.20
Total (anhydrous)	99.95	100.31	99.46	99.69	100.18	100.19	98.64	–	99.76	99.67	99.69
LOI	1.92	2.15	0.63	0.23	1.01	0.42	1.15	–	2.81	2.09	1.31
La	61.5	53.0	40.5	49.3	47.9	47.6	40.1	53.3	44.8	39.6	52.9
Ce	128.0	122.0	88.8	100.5	100.0	106.3	89.9	104.5	92.4	86.7	113.6
Nd	54.5	39.8	29.7	39.4	42.3	37.6	34.6	42.0	39.2	38.4	46.7
Sm	10.09	8.11	6.32	8.07	8.71	7.25	9.10	7.90	7.35	7.80	8.99
Eu	1.30	1.47	1.18	1.13	1.01	1.14	1.19	1.00	1.00	1.05	1.20
Tb	0.738	0.848	0.806	0.830	0.703	0.738	0.847	0.544	0.680	0.670	0.698
Yb	1.60	1.73	1.58	1.75	1.71	1.367	1.84	1.36	1.17	1.61	1.67
Lu	0.203	0.219	0.200	0.212	0.197	0.178	0.228	0.168	0.159	0.207	0.216
Y	17	17	21	17	17	13	21	–	13	16	17
Rb	271	210	168	251	261	271	120	–	246	244	267
Sr	266	319	342	279	231	290	239	237	262	315	226
Ba	416	630	537	596	484	551	511	428	639	496	328
Cs	37.0	264.3	11.0	18.4	21.6	107.3	39.3	19.9	21.9	16.8	28.3
U	14.1	8.9	4.8	13.4	14.8	8.8	17.0	14.1	12.7	12.9	14.3
Th	31.1	32.9	26.5	27.8	28.0	23.0	35.7	30.2	29.3	26.5	32.6
Pb	20.0	–	–	25	–	–	–	–	24	22	19
Hf	6.0	5.8	5.5	5.7	5.6	5.4	5.9	4.8	5.3	5.5	6.0
Zr	180	171	181	186	182	179	188	–	166	178	178
Nb	18	15	17	18	17	16	21	–	14	17	19
Ta	2.2	2.0	2.0	2.4	2.6	2.0	2.8	2.2	2.3	2.3	2.5
Sc	7.1	7.3	6.7	6.8	6.9	6.8	7.3	6.2	7.1	6.7	7.2
Cr	16	19	12	14	16	17	7	12	20	14	14
Ni	5	6	7	1	6	4	1		5	3	0
Co	7	51	7	28	6	5	6	6	7	6	6
Act Labs; ICP-MS analyses	Gd=5.21, Dy=3.53, Ho=0.62, Er= 1.74, Tm=0.25				Gd=5.02, Dy=3.64, Ho=0.64, Er= 1.84, Tm=0.27						
Latitude °S	26.048	25.985	25.839	26.126	25.666	25.703	26.044	26.050	26.034	25.975	25.975
Longitude °W	66.890	67.000	66.922	66.955	66.878	66.879	67.412	67.422	67.359	67.210	67.210
Elevation (m)	4813	4920	4576	4765	4240	4333		4305	4305	4920	4920
Notes	pumice	grey pumice-rich	pumice-rich	welded pumice-rich	crystal-rich whole rock	crystal-rich pumice	biotite-rich whole rock	pumice-rich	pumice	white pumice	pumice-rich

See Electronic Appendix Table A4 for this paper for complete data set for Intracaldera and Galán Group ignimbrites

Analytical methods discussed in Appendix 1

same Y contents in the Real Grande ignimbrite and high Y contents in the Galán ignimbrites. The analyses in Tables 2 and 3 and Electronic Appendix Table A4 further indicate that northern intracaldera tuffs are like the Real Grande ignimbrites and that the southern intracaldera tuffs have the lowest Rb/Sr ratios among Cerro Galán ignimbrites. Differences can also be seen within the REEs whose overall abundances are highest in the Galán ignimbrites (Figs. 4, 5a and 8). Figure 5b shows that the lowest La/Sm (<6) at the highest Sm/Yb ratios (>5) are in the Merihuaca and Real Grande ignimbrites, the lowest Sm/Yb ratios (~4) are in the Galán ignimbrites and that the Galán ignimbrites can cluster in regional fields. Figure 6 shows that there are no clear patterns in the negative Eu anomalies within the precision of the analyses. Figure 5c shows that the Galán ignimbrites generally have the lowest Zr/Nb ratios, the Real Grande ignimbrites the lowest Ba/Th ratios among the Toconquis ignimbrites and the far west Galán ignimbrites the lowest Zr/Nb and Ba/Th ratios of all of the Cerro Galán ignimbrites. Figure 5d shows that the Blanco and lower

Merihauca ignimbrites have the highest Ba/La and Ba/Ta ratios and that the lowest La/Ta ratios and Ba/Ta ratios are in the Galán ignimbrites.

The trace element differences among the Toconquis and Galán ignimbrites are emphasized when representative analyses are normalized to the analyses of Real Grande pumice sample SAF319p. As seen in Fig. 8, the Galán samples have the highest REE, Cs, Nb, Ta, Ti, Th and U concentrations and the lowest or similar Rb, K, Ba, Sr, Zr and Hf contents compared to the Toconquis samples. These differences are consistent with removal of sanidine, plagioclase, biotite and zircon from the Galán samples relative to the Toconquis samples. They cannot be due to crystal addition to the Galán ignimbrites as the most incompatible elements are highest and the most compatible elements lowest in the crystal-rich Galán samples. The most notable differences between the Real Grande and Merihuaca pumices are the lower Rb and higher Ba, Ta and U contents in the Merihauca pumices. The basal Merihauca pumice has notably lower concentrations of all elements except Ba and Sc.
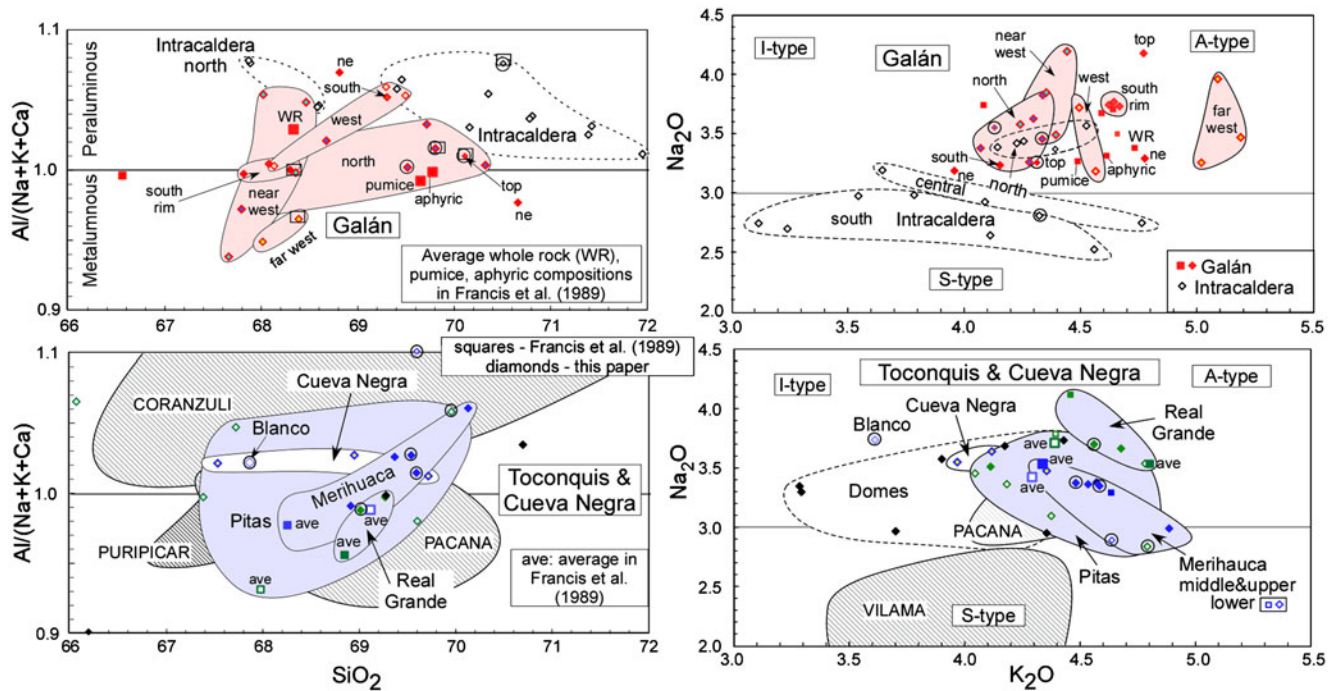
Fig. 3 Plots of molar Al(Na+K+Ca) ratios versus weight percent SiO₂ and weight percent Na₂O versus K₂O divided into fields for Toconquis (shaded - blue) and Cuevua Negra ignimbrites (white) in the bottom diagrams and Galán intracaldera (white) and Galán outflow (shaded - pink) units in the top diagrams. Analyses are for pumice and lithic-free whole rock samples. Square symbols are for data in Francis et al. (1989); average analyses for Galán pumice, aphyric and whole rock (WR) samples and Toconquis group pumice (ave) are labeled. Diamonds are for analyses from Tables 2 and 3 and Electronic Appendix Table A4; symbols and regions are as in Fig. 1: andesitic and dacitic domes (black points); Merihauca (dark blue; light blue centers are lower Merihauca); Pitas (dark green with light centers); Real Grande (green); intracaldera (open); Galán (red borders, centers coded as in Fig. 1). The plots show the metaluminous to marginally peraluminous and generally A-type granite nature of the ignimbrites. The Cerro Galán ignimbrites are the most Na-rich among large Puna-Altiplano ignimbrites; fields for northern Puna Coranzulí, Vilama, Puripicar and Atana ignimbrites (see Fig. 1) as compiled by Kay et al. (2008a) are shown for comparison. Circled samples are plotted in Fig. 4
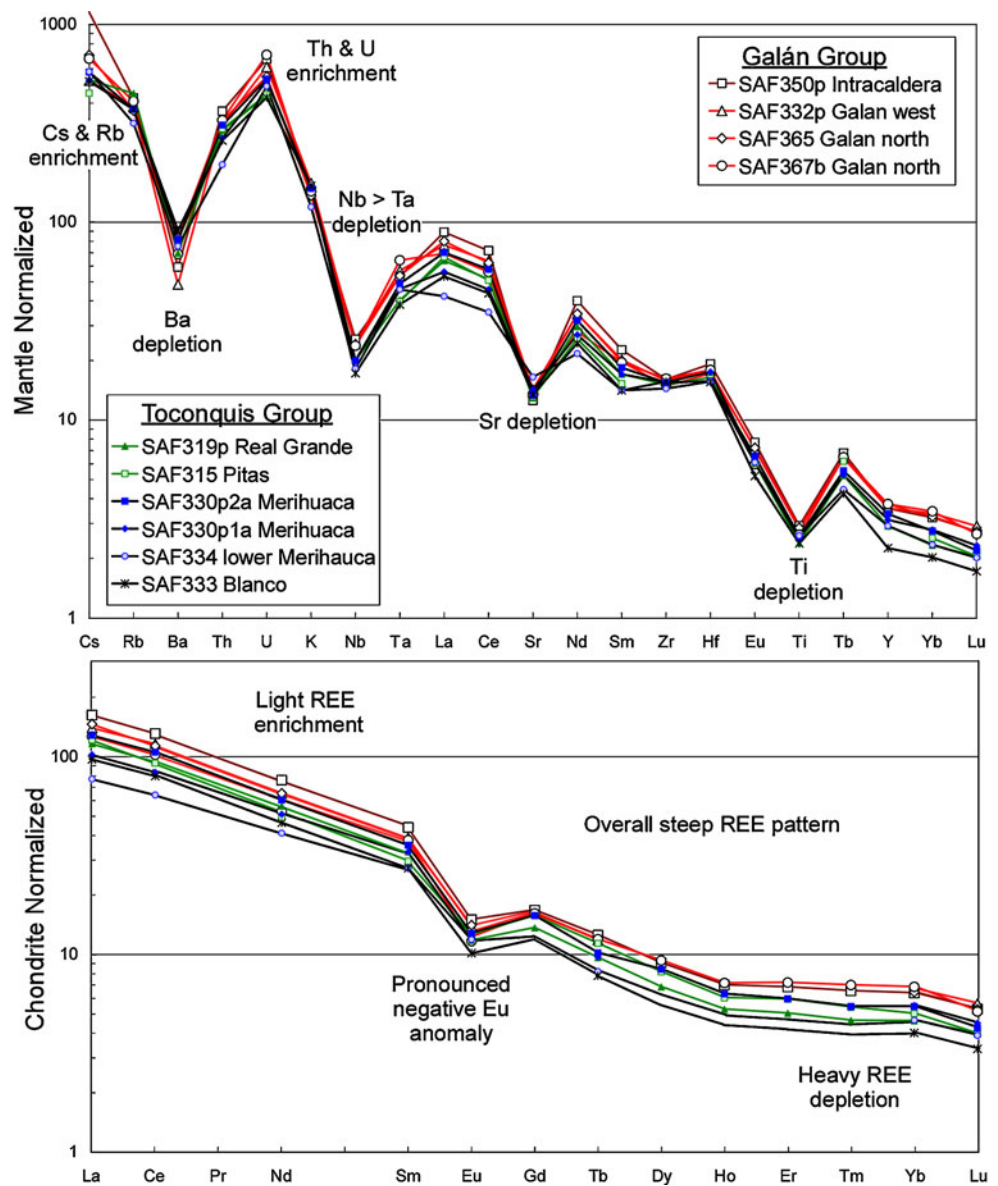
Sr and O isotopic ratios of the Cerro Galán ignimbrites

New $\delta^{18}O$ analyses measured on quartz in representative Toconquis group and Galán ignimbrites are listed with new and existing whole rock $^{87}Sr/^{86}Sr$ analyses from Francis et al. (1989) in Table 4. Analytical techniques are discussed Appendix 1. The $\delta^{18}O$ analyses on quartz are shown recalculated to $\delta^{18}O$ melt values by applying a quartz-melt fractionation correction of -0.3‰. Following Chang (2007), this correction is based on Bindeman et al. (2004)'s silica–dependent fractionation between melt and clinopyroxene ($\Delta px–melt=0.061\times[SiO2\ wt\%]–2.72$) and the cpx-qz fractionation of Chiba et al. 1989), which includes the effect of temperature ($\Delta qtz–px=2.75\times106\ T-2$) The resulting melt values [Merihuaca (+7.63‰); Real Grande (+8.04‰), intracaldera (+8.35‰) and Galán (+8.63‰–

8.85‰)} are substantially lower than the whole rock values (+11.8‰-+12.5‰) reported by Francis et al. (1989), most likely reflecting low-temperature alteration and secondary hydration of the ash matrix in the whole rock samples that they analyzed. The recalculated $\delta^{18}O$ melt values are plotted relative to Sr contents and $^{87}Sr/^{86}Sr$ ratios in Figs. 9 and 10 and provide mass-balance constraints (e.g. James 1981) in the discussion of the mantle and crustal components in the Cerro Galán ignimbrites below.

Discussion

Major and trace element, isotopic, and mineralogical characteristics are used below to examine the sources of the ignimbrite magmas and their evolutionary patterns.
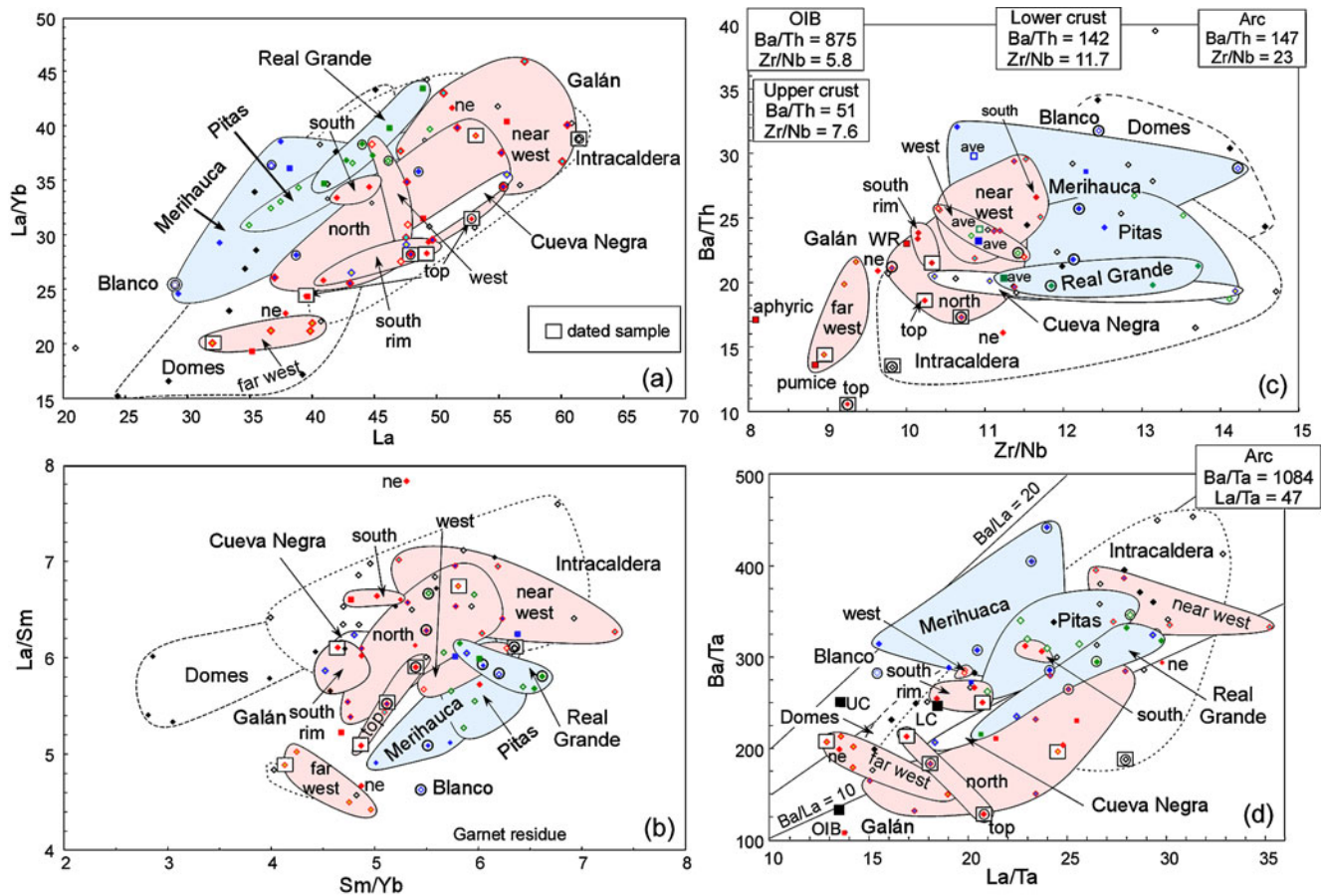
Fig. 5 Trace element plots showing some general chemical features of the dacite/andesite domes, Toconquis group ignimbrites and Galán intracaldera and outflow ignimbrites. Points enclosed in squares are samples with ages reported in Table 1. Other symbols and fields and the data sources are as in Fig. 3. Relative to the Toconquis ignimbrites, the Galán ignimbrites generally show the **a** highest La concentrations at a given La/Yb ratio, **b** highest La/Sm ratios at a given Sm/Yb ratio, **c** lowest Ba/Th and Zr/Nb ratios and **d** most intraplate-like Ba/La (<20) and Ba/Ta ratios. The highest Ba/La ratios are in the Blanco and lower Merihuaca ignimbrites. Plot (**b**) shows that Galán and Tonconquis ignimbrites have Sm/Yb ratios >4 requiring residual garnet. Representative values for OIB, arc, lower crust (LC) and upper crust (UC) from Sun and McDonough (1989) and Rudnick and Fountain (1995) are shown for reference. See discussion in text

Crystallization conditions are considered first followed by major and trace element constraints on depths and temperatures of magma evolution, the nature and proportions of mantle and crustal components and finally, a model is presented for the crustal evolution of the magmas that formed the Cerro Galán ignimbrites.

Crystallization conditions

Using coexisting magnetite and ilmenite pairs, Francis et al. (1989) calculated pre-eruption temperatures of near 800°–820°C for the Galán ignimbrites and up to 840°C for the Real Grande ignimbrite. These values are in line with those subsequently proposed for other large Puna ignimbrites (e.g., Lindsay et al. 2001; Soler et al. 2007). Another approach that can be used to estimate pre-eruption temperatures is to calculate zircon saturation temperatures from whole rock analyses. Using the formulation of Watson and Harrison (1983), zircon saturation temperatures are calculated at 799° to 823°C for the Toconquis ignimbrites, 802° to 823°C for the Galán ignimbrites and ~830°C n the welded zones of the Cueva Negra ignimbrite. As Francis et al. (1989) report traces of zircon in the Galán, Cueva Negra and Toconquis Real Grande ignimbrites, their pre-eruption temperatures would be less than 825°C. As zircon is not reported in the older Toconquis ignimbrites, temperatures of 799° to 823°C are a minimum pre-eruption estimate.

Pressures are more difficult to calculate. Francis et al. (1989) tried combining magnetite-ilmenite and coexisting feldspar temperatures to constrain pre-eruption pressures. Following work by Stormer and Whiney (1985) on the Fish Canyon tuff, they applied a pressure correction of ~18°C/kb to co-existing feldspar temperatures of 550° to 650°C to arrive at pre-eruption pressure estimates of 1-1.5 GPa for the Cerro Galán ignimbrites. However, this method has been questioned as the use of substantially lower pre-eruption

pressures for the Fish Canyon tuff based on the Al-in-hornblende barometer (near 0.23-0.25 GPa) bring calculated temperatures of 717°±33°C for sanidine ($Or_{69.6}$ $Ab_{26}An_{1.4}$) and of 750±17°C for plagioclase ($Or_{4.7}Ab_{64}An_{32.3}$) in the Fish Canyon tuff into line with those from coexisting oxide (760±30°C) and quartz-magnetite (762°C) geothermometers (see Bachmann and Dungan 2002). In comparison, average sanidine and plagioclase compositions that appear to be in equilibrium in the amphibole-free rhyodacitic Galán ignimbrites are $Or_{80.1}Ab_{18.7}An_{1.15}$ and $Or_{4.35}Ab_{61.65}An_{34.0}$ based on analyses in Francis et al. (1989). Using the SOLVCALC feldspar program of Wen and Nekvasil (1994), Galán feldspar compositions yield temperatures that range from 666° to 670°C at 0.1–0.25 GPa to 758° to 778°C at 1–1.2 GPa. Given pre-eruptions pressures for the Galán ignimbrites like those for the Fish Canyon tuff, Galán feldspars indicate pre-eruption temperatures near 670°C and record a different part of the evolutionary process than the ~800°C coexisting oxide temperature. The feldspars yield no clear constraints on pre-eruption pressures.

Other methods constrain the fO_2 and water content of the ignimbrite-forming magmas. Using coexisting oxides, Francis et al. (1989) calculated a fO_2 of -12 near 800°C, which is ~1.5 log units above NNO. This fO_2 is in the typical field for arc magmas and is consistent with estimates from FeO/MgO ratios (see plot in Sisson et al. 2002). The summary graph in Behrens and Gaillard (2006) shows that if biotite is the only mafic phase at a pressure of~3 kb near 800°C and the fO_2 is 2.5 units above NNO, the water content is~2.5–4%. If orthopyroxene coexists with biotite, temper-atures are>860°C and if hornblende is found with biotite, temperatures are<850°C and water contents >5%. The Eu/Eu* ratios near 0.45 to 0.65 in the Cerro Galán ignimbrites attest to feldspar fractionation under conditions that are not sufficiently oxidizing to reduce all Eu^{2+} to Eu^{3+}.

Major element considerations: the role of eutectic melts

Further information on temperatures and pressures of the Cerro Galán ignimbrites comes from plotting their whole rock weight percent CIPW norms on the Or-Ab-Qtz ternary diagram in Fig. 11a. As is common for silicic volcanic rocks, the Cerro Galán values plot on the Or side of the eutectic point, which is due in part to K from biotite being put in the calculated Or component. Overall, the Cerro Galán samples plot within the CIPW field of >90% of western US silicic magmatic rocks as compiled by Sisson et al. (2002) with the Galán points falling close to the average western US rhyolite and granite (Fig. 11b). The general variations in the eutectic with pressure are shown relative to the Cerro Galán points with the caveat that high boron and fluorine contents move the eutectic towards the Ab corner, whereas increasing the An contents moves the eutectic away (e.g., Wyllie et al. 1976). The Galán samples roughly fall between the eutectics for 0.2 and 0.5 GPa and the Merihuaca and Real Grande samples between the ones at 0.5 to 1 Gpa when compensation for the K in biotite is considered. All of the Cerro Galán samples fall within the general field for the 0.7 Gpa experiments of Sisson et al. (2002).
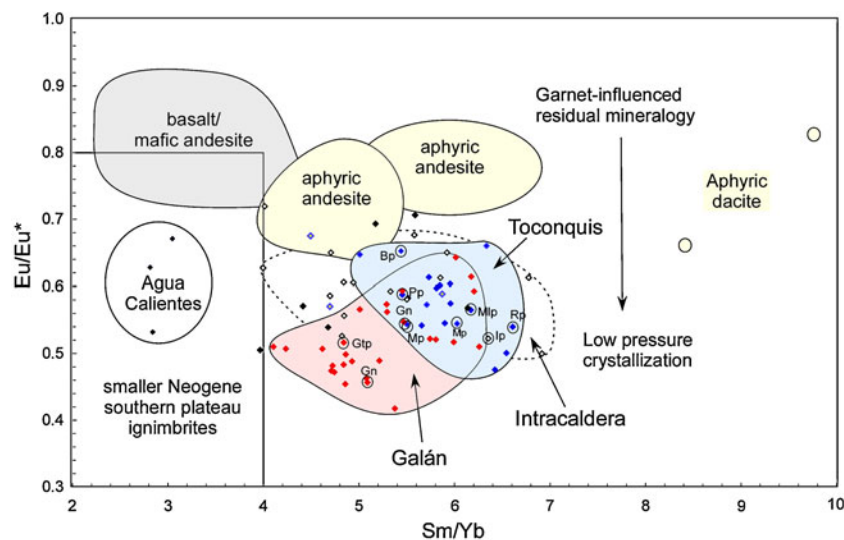

Fig. 6 Plot of Eu/Eu* versus Sm/Yb ratios for the Toconquis and Galán ignimbrites compared with fields for basaltic to mafic andesite, aphyric andesite and dacite flows and smaller Neogene ignimbrites in the region based on data compiled from Kay et al. (1994, 1999); Schnurr et al. (2007) and our unpublished data files. Plot illustrates the large negative Eu anomalies in Toconquis and Galán samples at high Sm/Yb ratios discussed in text. Symbols, fields and data sources for the Cerro Galán groups are as in Fig. 3. Circled points are for samples in Figure 3 where p indicates pumice (Bp:Blanco, Mlp:Merihauca, Mp:Merihauca, Pp:Pitas, Rp:Real Grande, Ip:Galán intracaldera, Gn: Galán north, Gtp : Galán top in west)
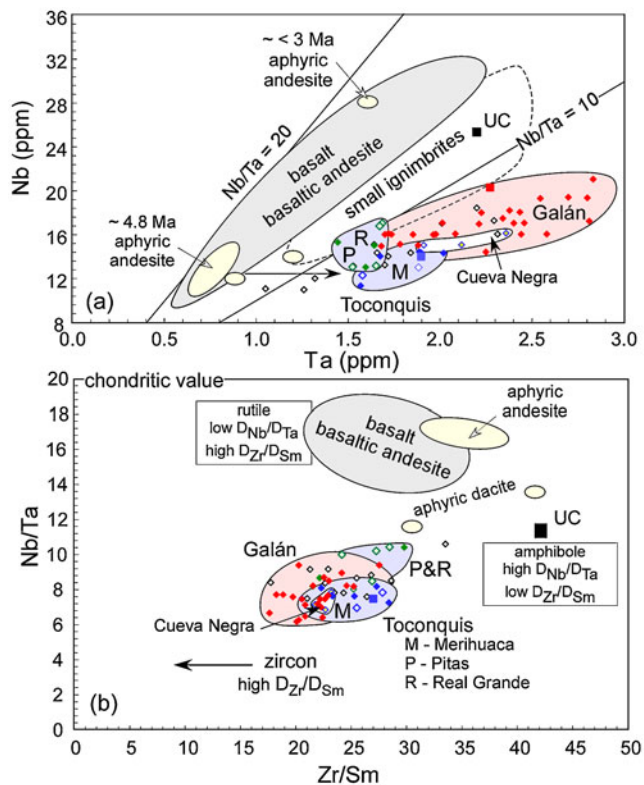
Fig. 7 Plots of (**a**) Nb versus Ta concentrations in ppm and (**b**) Nb/Ta versus Zr/Sm ratios for the Toconquis, Cueva Negra and Galán intracaldera and outflow ignimbrites relative to the fields for the same basaltic to mafic andesitic, aphyric andesite and dacite flows plotted in Figure 6. Plot (**a**) shows that the low Nb/Ta ratios in the Cerro Galán ignimbrites are principally due to a relative deficit in Nb compared to Ta. Plot (**b**) is consistent with the low Nb/Ta ratios being related to melts of residual amphibole (see Schmidt et al. 2004) and possibly accessory phases (discussion in text). UC is upper crust from Rudnick and Fountain (1995) and chondritic value and Nb/Ta and Zr/Sm distribution coefficient ratios are as discussed by Schmidt et al. (2004) and Münker et al. (2004). Fields, points and data sources are as in Fig. 3

Along with the arguments from the most incompatible trace elements discussed above (Fig. 8), plots comparing the CIPW proportions (Fig. 11a) of the Cerro Galán ignimbrites with modal data (Fig. 11b) from Francis et al. (1989) support the high crystal contents and presence of sanidine and quartz in the Galán ignimbrites as reflecting the retention of near-eutectic crystals in the Galán magmas. As shown in Fig. 11a, plotting the CIPW norms of the Toconquis and Galán ignimbrites with their CIPW plagioclase composition of $Ab_{81}An_{29}$, in lieu of Ab, displaces the points towards the An_{29} corner. As Galán ignimbrites have few mafic crystals and average plagioclase rim compositions are $\sim An_{34}$ (see Francis et al. 1989), the average plagioclase compositions in the Galán ignimbrites approach the rim and CIPW feldspar compositions. Therefore, the An29-Or-Qtz CIPW norm ratio of a completely crystallized Galán ignimbrite magma approximates a near eutectic modal composition. Figure 11b shows

that this same CIPW crystal ratio is near the normalized modal plagioclase, quartz and sanidine ratio in the Galán and intracaldera tuffs reported by Francis et al. (1989) and is not very different from the normalized modal crystal ratios from low residual least squares major element models relating Merihauca (M) and Real Grande (R) pumices to Galán (Gp) and intracaldera (Intra) pumices (points R to Gp and M to Ip in Fig. 11). Normalized crystal ratios from least squares models relating a Merihauca pumice to Galán western and northern outflow samples (points M to Gw and M to Gn) also plot near the CIPW ratio.

Thus, subtraction of near eutectic modal crystal proportions from the Toconquis magmas to form the Galán magmas can explain why the Galán magmas have higher incompatible element and generally similar major element compositions to the Toconquis ignimbrites. The retention of near eutectic crystal proportions in the Galán ignimbrites can also explain their higher crystallinity relative to the Toconquis ignimbrites. The greater crystallinity in the Galán ignimbrites is consistent with their final evolution just prior to eruption occurring at lower temperatures than for the Toconquis magmas.

Trace element considerations in shallow to deep level magmatic processes

Trace elements record properties of the magma source and evidence for the relative roles of the gain or loss of major and minor mineral phases, magma recharge and fluid and vapor transport. Comparisons among the Cerro Galán ignimbrites provide clues to both the shallow and deep processes that generated them.

The relative role of the gain or loss of the low pressure minerals present in the ignimbrites in shaping their trace element patterns is best revealed by models that use mineral/melt distribution coefficients (K_d). In practice, combining major element models that predict mineral differences between the Cerro Galán ignimbrites with mineral K_ds commonly suggested for rhyodacitic magmas produces problems in modeling elements like Sr, Ba and Eu. Ren (2004) and Zellmer and Clavero (2006) have recognized this problem elsewhere and discuss how highly variable and changeable K_ds for Sr, Rb, Ba and Eu in sanidine in silicic rocks makes K_d selection very difficult. An alternative is to normalize trace elements to a common sample and evaluate differences based on crystallization percentages from major element models and commonly expected trace element behavior in minerals. To do this, representative Cerro Galán samples are normalized to Real Grande pumice sample SAF319 in Fig. 8 (note dispersion from analytical errors on this non-logarithmic plot can be 5–7% or more). As a guide in qualitatively appraising mineral behavior, relative partition coefficients from Bachmann et al. (2005) for minerals in the Fish Canyon tuff are: a) plagioclase: Sr=2.5, Eu=3.1, Ba=
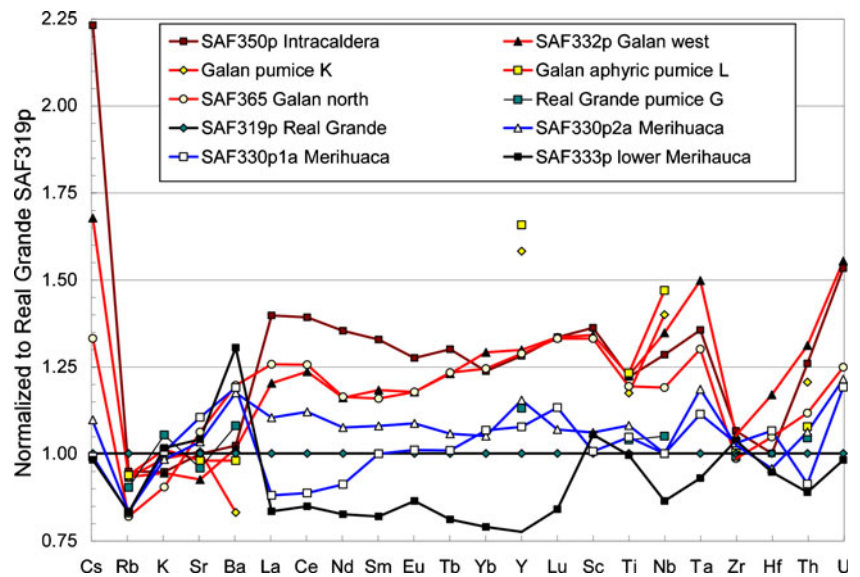
0.6, Pb=0.5, La to Sm=0.4 to 0.1; b) sanidine: Ba=17.1, Sr=7.4, Eu=2.9 and Rb=0.7; c) biotite: Ba=4.4, Sc=3.4, Nb=2.9, Rb=2.0, Ta=1.0. Eu to Gd=0.3 to 0.2; d) magnetite: Cr=1,290, Nb=0.37, Ni=86, Sc=0.21; e) zircon: Hf=3580, Yb to Sm=465 to 3.3, Ce=1.1, Y=181, U=48.6, Sc=151, Th=10.6, Cr=9.7, Nb=2.1, Ta=1.3.

Many of the major element differences between the Toconquis upper Merihauca and Real Grande pumices can be explained by a least squares model that removes 0.7% biotite, 5.4% plagioclase and 2.1% sanidine from the Real Grande pumice. The general trace element features in SAF330p2a in Fig. 8, which are qualitatively consistent with this model, are 5–10% increases in most moderately to strongly incompatible elements, and small variations in Sr and K and decreasing Rb contents indicating biotite, sanidine and plagioclase loss. Other differences can be attributed to source variability. A higher Ba content than expected can be explained by higher Ba/La ratios in the Merihauca ignimbrites (Fig. 5d), and the pattern of decreasing heavy to light REEs in SAF330p1a can be attributed to less residual garnet in the deep crust. The lower REEs, Nb, Ta and Th contents in basal Merihauca pumice SAF333p can be interpreted to reflect 10–20% less mineral fractionation relative to the Real Grande pumice. Higher Sc and Ti contents can be attributed to less biotite fractionation.

The trace element differences in Fig. 8 are more pronounced between the Real Grande and Galán ignimbrites. Largely incompatible elements including the REEs, Nb, Ta and Th are up ~17–25% in outflow samples SAF332p and SAF365 and up to ~35% in intracaldera pumice SAF350p. Y and Nb contents from averaged analyses of aphyric and crystal-bearing pumice analyses in Francis et al. (1989) are up as much as 65%. Little or no change in Hf and Zr reflects zircon fractionation from the

intracaldera magmas, lower P (Table 3) is due to apatite fractionation. Constant or lower Ba, Sr and Rb along with lower Na, K, Al and Ca contents indicate feldspar removal. The little commensurate decrease in Eu suggests oxidizing conditions under which Eu is largely Eu^{3+}. Larger increases in the heavy REEs (~35%) than in the light (~ 20%) and middle (15%) REEs in the outflow samples indicate some amphibole loss. Major element least squares models for outflow samples (R to Gp, M to Gw, M to Gn in Fig. 11b) indicate removal of 6–8% plagioclase, 5–7% sanidine, 1.5–4.5% quartz and 0–1.3% biotite), which is not enough crystallization to explain incompatible element increases. A major element least squares model relating Merihauca SAF330p2a to intracaldera pumice Saf350 (M to Ip in Fig. 11b) indicating a 30% loss of plagioclase, sanidine and quartz in near eutectic proportions is in line with increases in REE, Sc and Ta contents. Large increases in the most incompatible elements (up to 225% for Cs, >150% for U) require repeated magma injection and open system crystallization or enrichment by fluids.

A comparison of the two Galán outflow sample patterns in Fig. 8 shows a basic similarity in their REE patterns and differences in their incompatible elements. These observations, along with distinct sanidine and biotite $^{40}Ar/^{39}Ar$ ages support these ignimbrites coming from separate eruptions. The intracaldera deposits are more variable in composition consistent with multiple eruptions. A melt recharge by more mafic magmas at depth is required before the extracaldera eruptions to explain the lower trace element and silica concentrations in the outflow.

Among the common features of the Cerro Galán ignimbrites are large negative Eu anomalies (Eu/Eu*=0.45–0.55) and relatively steep heavy REE patterns (Sm/Yb=4.2–6.8) whose origins require separate explanations as they do not

correlate (Fig. 6). This lack of correlation is emphasized by the negative Eu anomalies in the Cerro Galán ignimbrites being similar or larger than those in smaller southern Puna ignimbrites with Sm/Yb ratios of 2–4 (Fig. 6, see Schnurr et al. 2007). The argument that the Eu anomalies are largely genetically independent from the crystals in the ignimbrites comes from the normalized plot in Fig. 8 on which the crystal-rich Galán ignimbrites show little difference in Eu level compared to the crystal-poor Toconquis ignimbrites. The simplest explanation is that the Eu anomalies in the Cerro Galán ignimbrites are generated at mid-crustal depths and are already present when the magmas reach, and further crystallize at the shallower level from which they erupt.

The high Sm/Yb ratios (Figs. 5b and 6) are consistent with garnet playing a role as a residual mineral and possibly as a fractionating phase at greater depth. This picture contrasts with that for the Fish Canyon tuff where Bachmann et al. (2005) argue that garnet is not needed as La/Yb (18–21) and Sr/Yb (17–24) ratios can be explained by hornblende and titanite, which are present in the ignimbrites. The difference in the Cerro Galán ignimbrites is that titanite has not been reported, hornblende is rare and La/Yb ratios are much higher (20–45) at similar Sr/Yb ratios (17–24). Further, Sm/Yb ratios higher than 5 in the Cerro Galán ignimbrites cannot be generated by amphibole fractionation alone. The similarity in Sr/Y ratios can be explained by feldspar fractionation from magmas with steep REE patterns inherited from depth. Corroborating evidence for involvement of deep crustal melting and assimilation comes from Pliocene aphyric dacites east of Cerro Galán (Fig. 1) with very steep heavy REE patterns (Sm/Yb ratios up to 8; Fig. 6; Kay et al. 1994, 1999; Kay et al. 2008b). Depletion of Sr and Eu by mid-crustal feldspar fractionation from magmas generated at greater depth where Sr and Eu are decoupled

can explain higher Sr contents (250–350 ppm) in the Cerro Galán ignimbrites than in smaller ignimbrites with the same Eu/Eu* (Fig. 6, Schnurr et al. 2007).

Another distinctive feature of all Cerro Galán ignimbrites is low Nb/Ta ratios (10-6), which are much lower than those in mafic lavas, aphyric andesites and dacites (19–14) and smaller ignimbrites (14 -11) in the region (Fig. 7a and b). These low ratios cannot be attributed to grinding contamination as the samples were prepared in agate and alumina oxide containers. As summarized by Schmidt et al. (2004) and Münker et al. (2004), common mineral phases with high enough mineral/melt distribution coefficients and concentrations to substantially separate Ta from Nb are rutile (K_dNb/K_dTa for rutile/melt~0.4–0.6) and titanite (titanite/melt K_dNb/K_dTa=0.3-0.4) and to a much lesser extent garnet (garnet/melt K_dNb/K_dTa=0.4–0.7). The most important mineral favoring Nb over Ta is amphibole (amphibole/melt K_dNb/K_dTa=1.3–1.6). Overall, melting of rutile-bearing eclogite lowers the Nb/Ta ratio in the residue, whereas low fraction melting of rutile-free garnet amphibolite or amphibole eclogite increases the Nb/Ta ratio in the residue (Schmidt et al. 2004; Goss and Kay 2009). Permissible models to contribute to low Nb/Ta ratios in the Cerro Galán magmas involve melting of restitic rutile-bearing eclogites with already low Nb/Ta ratios or low fraction melting leaving an amphibole-rich residue. The overall Nb/Ta depletion and low Nb/Ta ratios are consistent with melting of garnet-amphibolite with partition coefficients compiled by Foley (2004). However, such melting cannot explain Nb/Ta ratios <8, which could indicate the presence of an additional role for accessory phases such as zircon in melting and/or crystallization processes.

Other issues are the origin of the enrichment of very incompatible elements like U and Cs over slightly less

Table 4 Oxygen and Sr isotopic analyses

		$\delta^{18}O‰$		$^{87}Sr/^{86}Sr$	
Cerro Galán Ignimbrite Units.		quartz	magma calculated	measured	initial
Merihuaca	SAF330p2	+7.93	+7.63	0.711426	0.711218
Real Grande	SAF319p	+8.65	+8.35		
Galán intracaldera	SAF350p	+8.34	+8.04		
Galán west	SAF332b	+9.15	+8.85	0.71	0.711345
Galán north	SAF367a	+8.93	+8.63		
Cerro Galán Region Mafic Fows		olivine			
Cerro Chato flow	SAF32	+6.35[a]		0.706855	0.706850
Diablo flow	SAF24	+6.75[a]		0.705583	0.705568
Laguna Purulla flow	SAF76	+6.25[a]		0.71	0.706449

[a] Reported values are averages of two analyses

Ages and locations of mafic flows in Risse et al. (2008)

Sr isotopic analyses listed for SAF24 is from sample SAF25 in Kay et al. (1994)

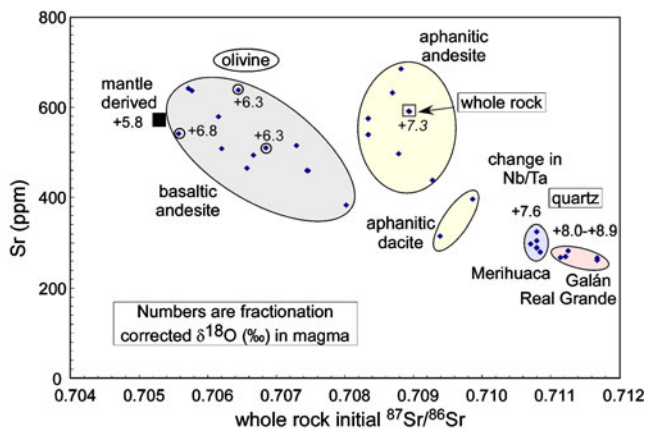Analytical methods and calculated $\delta^{18}O‰$ values discussed in Appendix 1

Fig. 9 Plot of $^{87}Sr/^{86}Sr$ ratios versus Sr (ppm) in Cerro Galán ignimbrites relative to compositions of mafic lavas, aphanitic andesites and dacites in the region. Mineral values recalculated to melt values based on $\delta^{18}O$ (‰) for olivine and quartz analyses are indicated. Data are from Table 4, Francis et al. (1989), Kay et al. (1994, 1999), Kraemer et al. (1999) and our unpublished data files

incompatible elements like Th in the Toconquis (Th~25–28, U~9–11, Cs 17–22 ppm) and Galán (Th~32, U~14, Cs 28–38 ppm) ignimbrites relative to the aphyric dacite lavas in the region (Th~26; U~5.5, Cs~6 ppm; Kay et al. 1999), and higher Rb contents (~ 200–300 ppm) relative to smaller ignimbrites in the area (< 200 ppm; Schnurr et al. 2007). U, Cs and Th systematics in apparently unaltered samples suggest that high U and Cs contents are largely due to crystal-melt equilibria. Evidence against alteration comes from clustering of analyses from different regions of the Galán ignimbrite on Cs versus Th or U plots (U/Cs from
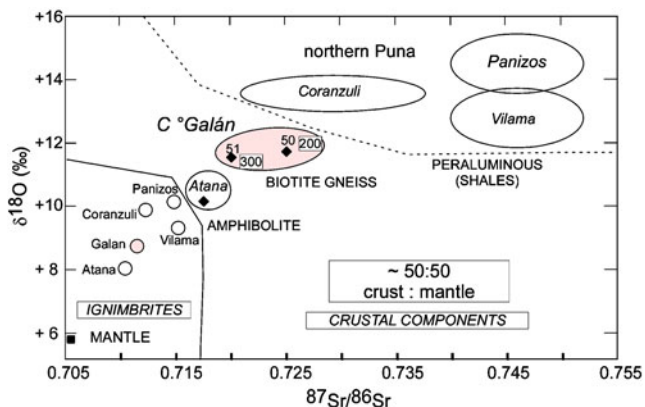
Fig. 10 Plot of $^{87}Sr/^{86}Sr$ versus $\delta^{18}O$ (‰) showing isotopic compositions of large volume Puna ignimbrites (open circles) and range of possible crustal contaminants mixed with a mantle-derived magma with a $^{87}Sr/^{86}Sr$ ratio of 0.7055, 550 ppm Sr and a $\delta^{18}O$= 5.7‰. Numbers near points in Cerro Galán field are crustal percentages needed to produce ignimbrite at the Sr content shown in box (see Table 5 and discussion in text). The results for the suite of Puna ignimbrites are discussed by Kay et al. (2008a) and the details will appear in another publication. Data are from Table 4, Francis et al. (1989), sources in Kay et al. (2008a) and our unpublished data files

0.5 to 0.9; Th/Cs from 1 to 3). Ratios in the Toconquis ignimbrites are<0.7 and>2 respectively. As expected for fractional crystallization, linear trends intersect the origin of a Cs-U plot and form a horizontal array on a Th/U versus Cs plot. As zircon takes U over Th, the Galán ignimbrites, which have lost zircon relative to the Toconquis ignimbrites would be even more U-rich (and Th-rich) if zircon had not been removed. Zircon in the Galán ignimbrites likely crystallized from the saturated melts along with feldspars and quartz. The high Cs and U contents and low Th/U ratios could be the result of incremental melt aggregations and open system magma processes. As an observation, the source of the Li in the Li-rich salts mined in the Salar de Hombre Muerto (Fig. 1) may be ultimately tied to the same enrichment processes as Li can come from leaching of glassy pyroclastic deposits.

Crustal and mantle sources of the Cerro Galán ignimbrites

Another issue in understanding the Cerro Galán ignimbrites is determining the relative contributions of mantle and crustal sources. Francis et al. (1989) argued that melting of the deep crust provided the most likely mechanism to explain the overall chemical similarities of the Cerro Galán ignimbrites over 4 million years along with Pb and Nd model ages of over 1.5 Ga. They ruled out melting of the local upper crust as this crust is too radiogenic to reconcile with the $^{87}Sr/^{86}Sr$ (~0.710–0.711) ratios in the ignimbrites. They discussed the alternative that the ignimbrites could be mixtures of crustal and mantle melts, but felt that the evidence, which included: 1) lower $^{87}Sr/^{86}Sr$ ratios in~ An66-60 plagioclase cores than in the whole rock, 2) a slight positive correlation between $^{87}Sr/^{86}Sr$ and Rb/Sr ratios, and 3) lower Nd than Pb model ages, was equivocal.

An important part of the evidence that Francis et al. (1989) used for a dominantly crustal source for the Cerro Galán ignimbrites was their whole rock $\delta^{18}O$ values of +11 to +12‰. The fractionation corrected $\delta^{18}O$ values based on analyses of quartz in Table 4 present a different picture. Given a $\delta^{18}O$ value of +5.8‰ for the mantle, magmatic values calculated from the quartz phenocryst data of +7.63‰ for the lower Merihuaca and an average of +8.47‰ from four analyses of the Real Grande and Galán ignimbrites (Fig. 9; Table 4), the crustal component would have values of +9.4‰ and +11.1‰ for a 50:50 ratio of crust to mantle-derived basalt (Fig. 10).

A 50:50 crust to mantle-derived basalt mixture is permissible with Sr AFC models using mantle-derived basalt with an $^{87}Sr/^{86}Sr$ ratio of 0.7055 and 550 ppm Sr and a crustal end-member with 0.720 to 0.725 and 300 to 200 ppm Sr (Fig. 10). The composition of the mafic end-member is based on arguments for enriched mantle producing late Neogene mafic magmas as first suggested by Rogers and

Hawkesworth (1989) for the southern Puna and expanded by Kay et al. (1994) and Kay (2006) for the southern CVZ (Fig. 1). The most logical Neogene enrichment process is the recycling of continental crust and lithosphere into the mantle by crustal delamination and forearc subduction erosion (e.g., Kay 2006; Kay and Coira 2009; Goss and Kay 2009). The values for the crustal end-members are calculated from Cerro Galán ignimbrite analyses by solving the three equations in Aitcheson and Forrest (1994), which they derived from the AFC equations of dePaolo (1981). These equations use different combinations of isotopic and concentration data from the parental magma, crustal assimilant and erupted magma. Together, they can be solved for r (rate of crustal assimilation/fractional crystallization), F (mass of magma remaining/original magma) and bulk crystal/melt Sr distribution coefficients (K_dSr) at different crustal levels. The first equation, which does not use the Sr content in the erupted

magma or F, gives the value of r if K_dSr is given. Based on the steep REE patterns and the high Sr contents in the Cerro Galán ignimbrites, K_dSr is set at 0.1 corresponding to conditions where feldspar is unstable. Observations from Central Andean volcanic rocks support this by suggesting that silicic Andean magmas fractionate from andesitic melts whose $^{87}Sr/^{86}Sr$ ratios are largely set in the deep crust (e.g., Aitcheson and Forrest 1994). Using this r, the other two equations can be solved for K_dSr. The second equation does not use any isotopic data and is strongly influenced by feldspar fractionation, which largely occurs at mid to upper crustal levels. The calculated K_dSr is near 1 as expected. The last equation does not use the Sr content of the crustal component and yields an intermediate K_dSr as expected. Two possible, but non-unique solutions of these equations with r at 0.50 and 0.51 and F at 0.42 and 0.48 yield the crustal end-members with $^{87}Sr/^{86}Sr=0.725$ at 200 ppm Sr
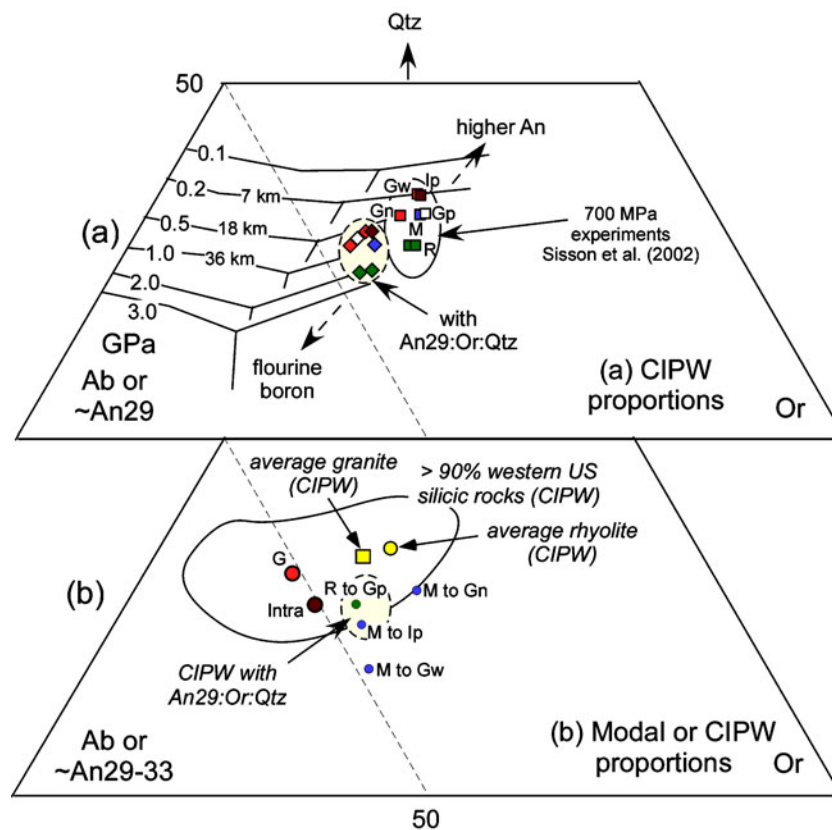

Fig. 11 Triangular plots of (a) CIPW weight percent normative compositions of Cerro Galán ignimbrites {Merihuaca SAF330p2a (M); Real Grande SAF319p and pumice G in Fig. 8 (R); Galán intracaldera SAF350p (Ip), Galán pumice K in Fig. 8 (Gp), north SAF365 (Gn), west SAF365 (Gw)} plotted as Ab-Qtz-Or (squares surrounded by solid line) and as An+Ab(~An 29)-Qtz-Or (diamonds surrounded by dashed line) on the granite ternary diagram, and (b) modal proportions of quartz, sanidine and plagioclase from average data for the Galán outflow (G) and intracaldera (Intra) ignimbrites in Table 1 in Francis et al. (1989), and least squares mixing models between Merihuaca (M) and Real Grande (SAF319p–R) pumices and

Galán ignimbrites (Gn, Gp, Gw and Ip) discussed in text. The dashed field is the same as in (a). Also shown in (b) are the CIPW compositions (Ab-Or-Qtz) of average granite (yellow square) and rhyolite (yellow circle) in the western US and the field encompassing >90% of western US silicic rocks as plotted by Sisson et al. (2002). The change in position of the Ab-Or-Qtz eutectic position with pressure and direction trends with increasing boron, fluorine and An content in (a) are as in Wyllie et al. (1976). The oval field in white in (a) encloses the CIPW norm compositions of 700 MPa melting experiments with compositions like the Galán ignimbrites in Sisson et al. (2002)

Table 5 Parameters in Aitcheson and Forrest (1994) equations

		Sr ppm	$^{87}Sr/^{86}Sr$	r	F	KdSr Equation VI	KdSr Equation VII	KdSr Equation VIII
Crustal component	Model 1	200	0.7250	0.50	0.42	0.10	0.88	0.49
Crustal component	Model 2	300	0.7200	0.52	0.48	0.10	1.07	0.53
Mantle-derived basalt		550	0.7055					
Cerro Galán Ignimbrite		270	0.7115					

and $^{87}Sr/^{86}Sr=0.7200$ at 300 ppm Sr (Fig. 10: Table 5). The F and K_dSr values in these solutions are compatible with those for a backarc Andean basalt at 1 GPa ($K_dSr\sim0.57$ at $F=0.5$ and ~0.73 at $F=0.4$) and 0.7 GPa (K_dSr is~0.91 at $F=0.6$ and ~1.14 at $F=0.5$) calculated with the MELTS program by Caffe et al. (2002). The modeling allows near 50:50 mixtures of enriched basalts and melted Grenville to Paleozoic age amphibolite and plutonic rocks consistent with the regional basement. Near 50/50 mixtures of a similar mafic magma with regionally variable crustal melts are also permissible in explaining the compositions of other Puna ignimbrites to the north (Kay et al. 2008a).

Some chemical features of the Cerro Galán ignimbrites appear to reflect local and regional trends in Puna volcanic rocks consistent with the basalt mixing end-member reflecting the mantle source (Fig. 1). Based on ages published and compiled by Risse et al. (2008), contemporaneous southern Puna flows include 7-6.6 Ma basaltic andesites, 4.8- 4.1 Ma mafic andesite, andesite and dacite flows, and 2.5 to 0.3 Ma mafic flows. Support for a decreasing influence of a subduction-related component in the backarc over a steepening subduction zone during this period comes from La/Ta ratios of ~55 and Ta contents<1 ppm in~4.8 Ma aphyric andesites, La/Ta ratios of ~30 and Ta>1.5 ppm in~2 Ma aphyric andesite and La/Ta ratios as low as 18 in the youngest flows (Fig. 7, Kay et al. 1994, 1999). Relatively high Ba/Ta ratios in the Merihauca ignimbrites (Fig. 5d) could also reflect this trend as could the observation that the Toconquis ignimbrites are the most arc-like among Cerro Galán ignimbrites, which all plot near the volcanic arc/ syncollisional boundary on Nb, Ta, Y, Yb and Rb-based granite discrimination diagrams. On a broader scale, the Galán ignimbrites have the most intraplate-like La/Ta ratios among Puna ignimbrites (Coira et al. 1993; Kay et al. 1999, 2008a) in accord with the most intraplate-like Neogene mafic flows erupting in the southern Puna (Kay et al. 1994, 1999). Ba/La ratios<20 in the southern Puna mafic flows (Fig. 5b; Kay et al. 1994, 1999) and the Cerro Galán ignimbrites are in accord with little to no arc fluid contribution to a thickening backarc mantle wedge (Kay and Coira 2009). Fractionation of sanidine is also a factor in producing low Ba/La ratios in the ignimbrites, particularly in the Galán ignimbrites (Fig. 5d).

Crustal evolution of the Cerro Galán ignimbrites

Figure 12 shows a schematic cross section through the subducting plate, mantle wedge and crust within the general framework of geophysical constraints in the southern Puna (Heit 2005; Wölbern et al. 2009) and inferences from the northern Puna. The magmas that erupt as ignimbrite are shown as evolving at three levels: melting and hybridization in the lower crust, accumulation of crystal mushes in the mid crust and eruption from ephemeral shallow level magma chambers.

As discussed by Coira and Kay (1993) and Kay et al. (1999), melting takes place in the mantle wedge producing basaltic magmas that pond, infiltrate and partially melt the lower crust. The intrusion of mafic magmas into the crust and partial melting of the base of a thickened crust has been considered by Dufek and Bergantz (2005), who argue that overlapping basaltic intrusions into an amphibolitic basal crust is an effective way to produce crustal melts that mingle with fractionating mafic magmas. Melts of amphibolite can generate the high La/Yb ratios and contribute to the low Nb/Ta ratios in the ignimbrites by leaving a garnet-amphibole bearing residue at pressures above 1 to 1.2 GPa. This process results in andesitic/dacitic magmas that migrate upwards leaving a residual garnet pyroxenite that is denser ($>3,300$ kg/m^3) than the underlying peridotite and is subject to delamination. This is the high pressure stage for the AFC models above.

The deep crustal hybrid melts are shown rising through the crust and accumulating near 20 km depth in accord with the seismic receiver function image in Wölbern et al. (2009). Yuan et al. (2000) interpret the top of the receiver functions as the upper limit of fluids and melts and the bottom as the upper boundary of dry, hot refractory crust that has lost melts and volatiles. The picture in Fig. 12 differs from the two published thermal models for generation of Puna ignimbrites. A difference with the Babeyko et al. (2002) model is that significant amounts of mantle melt enter the crust rather than ponding at the base. Their models require almost 20 million years before melts are established near 20 km at temperatures near 800°C, a time frame that does not work well in the southern Puna where magmatism begins at ~14 Ma and big Toconquis ignimbrites are erupting
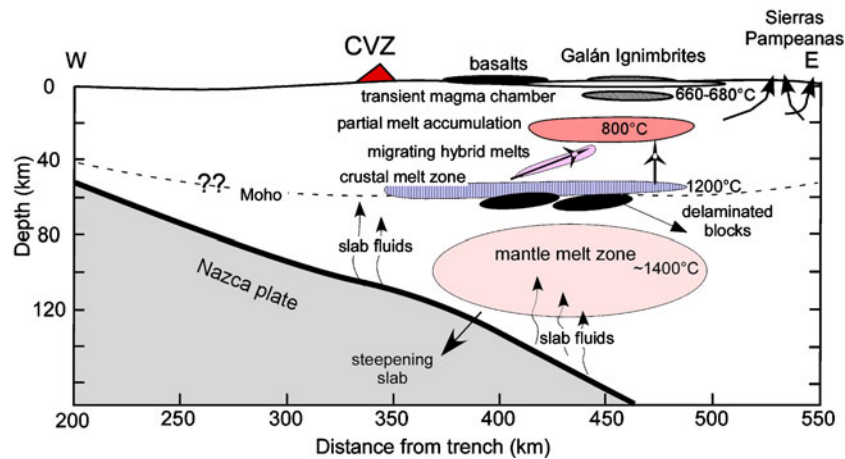
Fig. 12 Mantle and crustal scale cross-section illustrating the mantle and three stage evolution model for the Cerro Galán ignimbrites discussed in the text. Crustal melt zones and migrating melt pathway (arrows and purple zone) are based on seismic P-wave receiver function images in Heit (2005) and Wölbern et al. (2009). Crustal thickness is from Heit (2005) and McGlashan et al. (2008). Slab dip is that used by Kay et al. (1994). Temperatures are estimates or from the geothermometry in the text. Section shows hydration above steepening slab enhancing melting of a thickening mantle wedge above a steepening slab producing basaltic melts that pond and enter the ~60 km thick crust. Mantle and crustal hybrid melts are produced in the lower crustal melt zone (*blue zone*) as the mafic magmas partially melt the crust leaving a residual garnet-bearing lower crust. The hybrid magmas percolate up and accumulate in mush zones with temperatures near 800°C (*red zone*) like those imaged on Puna seismic images. The melts partially crystallize in the mush zone which is recharged from below. Regional contraction related to the uplift of the Sierras Pampeanas (*arrows* represent generalized east and west-verging high angle reverse faults) causes rhyodacite melts to segregate and accumulate in shallow level (*striped*) chambers where they are subjected to various degrees of near eutectic crystallization before erupting. Delamination (or *foundering*) of garnet-bearing residues (*black lens*) causes renewed decompression melting and new injections of basaltic magmas that possibly trigger the ignimbrite eruptions

by 4.8 Ma. An appealing aspect of their model is that crustal melts rise in narrow channels that stabilize in the same region for several million years. The initial conditions in which lithospheric delamination or a steepening subduction zone in a contractional stress regime brings heat flow to 60 mW/m^2 at the base of the crust fits well with models for the southern Puna (Kay et al. 1994, 1999) in which the subduction zone steepens after the subducting Juan Fernandez Ridge on the Nazca plate has passed to the south (Kay and Coira 2009). In the model of de Silva and Gosnold (2007) for northern Puna ignimbrites, mantle-derived magmas enter the crust and pond near 30 km where they hybridize with mid-crustal melts and then accumulate in a 1-2 km thick crystal mush layer in a zone of neutral buoyancy near 19 km. A problem with this model is how to explain the steep REE patterns in the Cerro Galán ignimbrites.

By the mid-crustal stage, the melts in the crystal mush zone have essentially acquired their isotopic signatures, and the crystal extraction that generates the large Eu anomalies and trace element enrichments and differences between the ignimbrites is occurring. The Toconquis ignimbrites reflect periodic evacuations of evolved magma from the crystal mush layer at temperatures above the zircon saturation temperatures at a time of a high rate of basaltic intrusion into the base of the crust as inferred from an age peak in mafic lavas at this time (Risse et al. 2008). The feldspars producing the negative Eu anomalies and contributing to the depletion of Ba are left in the mush zone with the residual interstitial melt. This mush zone is then recharged from depth with increasing temperature producing melts of more refractory crust, which should have lower trace element concentrations. However, the period between the large Toconquis Real Grande and Galán eruptions from 4.68 Ma to 2.1 Ma appears to be a time of slower growth and significant crystallization in the mush zone resulting in large incompatible element increases in the melt. Differences in Cs and U concentrations allow more than 200% more crystallization (Fig. 8). Zircon crystallization in the Galán magmas reflects a decreasing temperature, possibly with increasing oxygen fugacity suppressing development of larger Eu anomalies despite evidence for more feldspar fractionation. The crystals left behind when the Galán magmas are extracted leave a significant plutonic component in the mid crust. The drop in incompatible element concentration between the Galán extracaldera and intracaldera ignimbrites is consistent with faster recharge of mafic magmas at the base of the crust producing more silicic melt accumulation in the mid crust. Advanced fractional crystallization of accessory phases at shallow levels results in enhanced depletion of nominally incompatible elements

The transfer of melts from the mush zone to magma chambers at 4–8 km could be triggered by regional contraction near the time of uplift of the Sierra Pampeanas

to the east (Figs. 1 and 12). Contraction would facilitate squeezing out low density melt from the mush zone, which would in turn ascend to a level of neutral buoyancy higher in the crust. This uplift, which began at 6-5 Ma, occurred in an out-of-sequence order on steep east- and west-dipping reverse faults (see Deeken et al. 2006). The early uplift could be linked with different phases of the Toconquis eruptions, and the younger faults further to the east to the Galán extracaldera and intracaldera ignimbrites. Boyce and Hervig (2008) present evidence from zoning in apatite for an increase in temperature just prior to eruption, which they speculate is due to injection of basalt into the crust.

The near eutectic crystals in the erupted magmas largely formed in these upper level magma chambers. The Galán magmas could have been removed in shortly dispersed batches leading to a series of closely spaced eruptions in line with their small chemical and age differences. Cooler temperatures in smaller magma chambers can explain their higher percentage of near-eutectic crystal formation than in the Toconquis ignimbrites. Older $^{40}Ar/^{39}Ar$ biotite ages could reflect their extraction along with complexly zoned plagioclase crystals as antecrysts from the mush zone rather than crystallization in the upper level magma chambers. Final pre-eruption pressures near 110 to 220 MPa are predicated on melt inclusion data from northern Puna ignimbrites that fit near isobaric cooling paths from 830°C in shallow reservoirs and equilibration pressures of high-Si rhyolitic glass (Schmitt 2002). De Silva and Gosnold (2007) argue that the brittle-ductile transition, which they define as the 450°C isotherm, moves upwards producing a very thin crustal lid that is breached when eruption occurs. Assimilation and blending of phenocrysts, antecrysts and xenocrysts occurs in the final chamber-wide convection at shallow levels in the last 10,000 years before eruption (Charlier et al. 2007).

The revised volume estimates of Folkes et al. (2010) of ~667 km³ and ~550 km³ for the Galán and Toconquis ignimbrites result in a total erupted volume of 1,217 km³. Given a 4.5 to 1 intrusive to extrusive ratio (e.g., White et al. 2006), nearly 6700 km³ of silicic magma needs to be generated. With a caldera area of 26 by 38 km (Folkes et al. 2010), an equivalent 5.5 km thick pluton is left at depth. Given dispersal over the area where the mafic lavas occur (~ 130 km north-south by 60 km east-west or ~7800 km², see Fig. 1 and Kay and Coira 2009), which is similar to the area of the ignimbrite deposits, an average thickness of 700 m of plutonic material is left behind. With a one to one crust to mantle melt ratio in the ignimbrites, ~5480 km³ of new mantle magma needs to be added over 4 Ma. This is equivalent to a magma production rate of 28 km³/km/Ma over 100 km and is near global arc magma production estimates that range from 30 to150 km³/km/Ma (see Jicha et al. 2006).

Conclusions

1) Single crystal $^{40}Ar/^{39}Ar$ sanidine ages, which are systematically younger than $^{40}Ar/^{39}Ar$ biotite ages, provide the best estimate of the eruption ages for the Galán ignimbrites and are consistent with an intra-caldera deposit at~2.13 Ma and at least two outfows; one to the west at ~ 2.09 Ma and one to the north at ~ 2.06 Ma. The eruption of the Galán ignimbrites in a series of events is supported by subtle, but systematic regional differences in the trace element chemistry of these ignimbrites. More detailed studies are needed to precisely determine the exact number and extent of Galán ignimbrites eruptions.

2) Evidence for a mantle-derived basaltic melt entering and melting the crust to produce hybrid melts that evolve into the ignimbrite magmas comes from Sr AFC models coupled with $\delta^{18}O$ analyses of quartz. $^{87}Sr/^{86}Sr$ ratios of ~0.7110 to 0.7116 and $\delta^{18}O$ values of +7.6 to +8.9‰ in the Cerro Galán ignimbrites are consistent with near 50:50 mixtures of an enriched basalt with $^{87}Sr/^{86}Sr=0.7055$ and 500 ppm Sr and a crustal component with $\delta^{18}O$ of +9 to +11‰ and $^{87}Sr/^{86}Sr$ from 0.720-0.725 at 300-200 ppm.

3) Substantial negative Eu anomalies, low Nb/Ta ratios, steep REE patterns, incompatible element enrichments and differences in crystallinity of the Cerro Galán ignimbrites reflect evolution at three crustal levels. High Sm/Yb ratios indicate melting of amphibolite by mantle-generated basalts producing hybrid melts and leaving residual garnet in the deep crust. Although the mechanism of producing Nb/Ta ratios <10 requires further study, these ratios are compatible with a hornblende residue in addition to a possible additional role for an accessory phase. However these low ratios are produced; they are not present in the smaller volume Puna ignimbrites. Incompatible trace element enrichments, high Rb/Sr and low Th/U ratios and negative Eu anomalies reflect melt recharge and crystallization in mush zones near 20 km at~800–840°C, followed by partial removal of the mush to shallow levels where variable degrees of near eutectic crystallization with little crystal separation occurs before eruption. Differences in trace element ratios and concentrations are enhanced by larger amounts of crystallization and incremental recharge of the mush zones with the strongest elemental enrichments occurring in the~2.5 million interval between the Galán and Toconquis ignimbrites. Higher temperatures in the Toconquis ignimbrites are reflected in less near-eutectic crystallization. Extraction of biotite and feldspar from the mush zone shortly before eruption can help to explain the older $^{40}Ar/^{39}Ar$ biotite ages as well

as complexly zoned plagioclase grains, and new sanidine crystallization at shallow depth can explain why sanidine gives younger ^{40}Ar/^{39}Ar ages. Crystallinity differences in the erupted ignimbrites are attributed to transport of biotite and other crystals from the mush zone at 800°C and variable amounts of near eutectic crystallization at temperature near 680°C in higher level chambers.

4) Episodic delamination of gravitationally unstable lower crust and injection of mantle basaltic magmas whose evolving chemistry reflects evolution over a steepening subduction zone could trigger the repeated eruptions of the Cerro Galán ignimbrites, as well as those to the north (Kay and Coira 2009).

Appendix 1: analytical methods

Whole rock major and trace element analyses in Tables 2 and 3 and Electronic Appendix Table A4 are reported on an anhydrous basis. Major elements, Y, Rb, Pb, Zr and Nb were analyzed at the Universidad de Jujuy using standard XRF procedures with USGS standards. Other trace elements and Na$_2$O were analyzed on whole rock powders by Instrumental Neutron Activation Analyses (INAA) at Cornell University. The Fe content of each sample was used as an internal flux monitor in the INAA analyses. The absolute element concentrations reported in the INAA analyses are ratioed to the FeO content in the XRF analyses. Na/Fe ratios in the XRF and INAA are generally in good agreement as are Sr, Cr and Ni concentrations. Where Ba analyses differed, INAA analyses are reported. INAA precision and accuracy based on replicate analyses of internal standards are 2–5% (2 sigma) for most elements and 10% for Sr, Nd and Ni at low concentrations. Gd, Dy, Ho, Er and Tm analyses on selected samples were obtained commercially at ACTLABS using their fusion ICP-MS package.

^{87}Sr/^{86}Sr isotopic ratios were measured on a VG Sector thermal ionization mass spectrometer (TIMS) at Cornell University using W single filaments and a quadruple collector dynamic procedure. The average value for standard NBS987 was 0.710221 (±0.0000044). Typical errors on single analyses are ±0.000005 to ±0.00008.

Oxygen analyses on phenocrysts were done on a Finnigan-MAT Deltaplus mass spectrometer with a Finnigan GC II continuous flow inlet system combined with a CO$_2$-laser fluorination line at Gottingen University (after Wiechert et al. 2002). The precision of the analyses is typically ±0.2. Samples are loaded into 2-mm deep holes in a nickel disk placed at the bottom of a sample chamber filled with surplus fluorine gas and then hit with a CO2 laser until sufficient silicate-bonded oxygen is released. The oxygen is cleaned by reacting surplus fluorine with NaCl and freezing the chlorine in liquid nitrogen cooled trap. The sample oxygen is next expanded into a vacuum extraction line and cryo-focused onto a 5Å molecular sieve, and then injected into a helium carrier gas flow by heating the molecular sieve to 100°C using boiling water and flushing through a gas chromatography capillary column into the mass spectrometer where the isotopic ratio is measured directly on molecular oxygen. Nine analyses of garnet standard UWG-2 (δ18O=+5.8‰), which was analyzed in each session, yielded 5.72±0.15‰. Data are reported in the δ-notation relative to standard mean ocean water (SMOW; ^{18}O/^{16}O=3.7990×10-4). Following Chang (2007), the fractionation correction for quartz is about 0.3‰ for Δqtz–melt.

References

Aitcheson SJ, Forrest AH (1994) Quantification of crustal contamination in open magmatic systems. J Petrol 35:461–488

Bachmann O, Dungan MA (2002) Temperature-induced Al-zoning in hornblendes of the Fish Canyon magma, Colorado. Am Min 87:1062–1077

Bachmann O, Dungan MA, Bussy F (2005) Insights into shallow magmatic processes in large silicic magma bodies: the trace element record in the Fish Canyon magma body, Colorado. Contrib Mineral Petrol 149:338–349

Babeyko AY, Sobolev SV, Trumbull RB, Oncken O, Lavier LL (2002) Numerical models of crustal scale convection and partial melting beneath the Altiplano-Puna plateau. Earth Planetary Science Lett 199:373–388

Behrens H, Gaillard F (2006) Geochemical aspects of melts: volatiles and redox behavior. Elements 2:275–280

Bindeman IN, Ponomareva VV, Bailey JC, Valley JW (2004) Volcanic arc of Kamchatka: a province with high-δ18O magma sources and large-scale 18O/16O depletion of the upper crust. Geochim Cosmochim Acta 68(4):841–865

Boyce JW, Hervig R (2008) Magmatic degassing histories from apatite volatile stratigraphy. Geology 36:63–66

Caffe PJ, Trumbull RB, Coira BL, Romer RL (2002) Petrogenesis of early Neogene magmatism in the northern Puna: implications for

magma genesis and crustal processes in the Central Andean Plateau. J Petrol 43:907–942

Chang Y-H (2007) O-Isotopes as tracer for assimilation processes in different magmatic regimes (El Misti, S. Peru and Tapaaca, N. Chile), Diplom Thesis, 51 pp, Göttingen

Charlier BLA, Bachmann O, Davidson JP, Dungan MA, Morgan DJ (2007) The upper crustal evolution of a large silicic magma body: evidence from crystal-scale Rb/Sr isotopic heterogeneities in the Fish Canyon magmatic system. Colo J Petrol 48:1875–1894

Chiba H, Chacko T, Clayton RN, Goldsmith JR (1989) Oxygen isotope fractionations involving dioside, forsterite, magnetite, and calcite: application to geothermometry. Geochim Cosmochim Acta 53:2985–2995

Coira B, Kay SM, Viramonte J (1993) Upper Cenozoic magmatic evolution of the Argentine Puna—a model for changing subduction geometry. Int Geol Rev 35:677–720

Coira B, Kay SM (1993) Implications of Quaternary volcanism at Cerro Tuzgle for crustal and mantle evolution of the Puna plateau, central Andes. Contrib Mineral Petrol 113:40–58

Deeken A, Sobel ER, Coutand I, Haschke M, Riller U, Strecker MR (2006) Development of the southern Eastern Cordillera, NW Argentina, constrained by apatite fission track thermochronology. From Early Cretaceous extension to middle Miocene shortening. Tectonics 25:TC6003. doi:10.1029/2005TC001894

DePaolo DJ (1981) Trace element and isotopic effects of combined wallrock assimilation and fractional crystallization. Earth Planetary Sci Lett 53:189–202

de Silva SL, Gosnold WD (2007) Episodic construction of batholiths: Insights from the spatiotemporal development of an ignimbrite flare-up. J Volcan Geot Res 167:320–325

Dufek J, Bergantz G (2005) Lower crustal magma genesis and preservation: a stochastic framework for the evaluation of basalt–crust interaction. J Petrol 46:2167–2195

Foley S (2004) A trace element perspective on Archean crust formation and on the presence or absence of Archean subduction. In: Condie KC and Pease V (eds.) When did Plate tectonics begin on Planet Earth? Geol Soc Am Spec Paper 440:31–50

Folkes CB, Wright HM, Cas RAF, de Silva S, Lesti C, Viramonte JG (2010) A re-appraisal of the stratigraphy and deposit volumes in the Cerro Galán volcanic system, NW Argentina. Bull Volcan: this volume

Francis PW, Sparks RSJ, Hawkesworth CJ, Thorpe RS, Pyle DM, Tait SR, Mantovani MS, McDermott R (1989) Petrology and geochemistry of volcanic rocks of the Cerro Galán caldera, northwest Argentina. Geol Mag 126:515–547

Goss A, Kay SM (2009) Extreme high field strength element (HFSE) depletion and near-chondritic Nb/Ta ratios in Central Andean adakite-like lavas (27º S, 68º W). Earth Planetary Sci Lett 270:97–109

Heit BS (2005) Teleseismic tomographic images of the Central Andes at 21º S and 25º.5 S: an inside look at the Altiplano and Puna plateaus, PhD thesis, Freien Universität, http://www.diss.fu-berlin.de/2005/319/indexe.html, Berlin, Germany

Hora JM, Singer BS, Jicha BR, Beard BL, Johnson CM, de Silva S, Salisbury M (2009) Biotite-sanidine $^{40}Ar/^{39}Ar$ age discordances reflect Ar partitioning and pre-eruption closure in biotite. Geol Soc Am Abstracts with Programs 41(7):421

James DE (1981) The combined use of oxygen and radiogenic isotopes as indicators of crustal contamination. Ann Rev Earth Planet Sci 9:311–344

Jicha BR, Scholl DW, Singer BS, Yogodzinski GM, Kay SM (2006) Revised age of Aleutian island arc formation implies high rate of magma production. Geology 34:661–664

Kay SM (2006) Chemical and isotopic evidence for modification of the Central Andean arc mantle by crust removed by forearc subduction erosion. Geochim Cosmochim Acta 170:A385

Kay SM, Coira BL (2009) Shallowing and steepening subduction zones, continental lithospheric loss, magmatism and crustal flow under the central Andean Altiplano-Puna plateau. In Kay SM, Ramos VA, Dickinson WR (eds) Backbone of the Americas: Shallow subduction, plateau uplift and ridge and terrane collision. Geol Soc Am Memoir 204:229–260

Kay SM, Coira B, Viramonte J (1994) Young mafic back-arc volcanic rocks as indicators of continental lithospheric delamination beneath the Argentine Puna plateau, Central Andes. J Geophys Res 99:24323–24339

Kay SM, Mpodozis C, Coira BL (1999) Magmatism, tectonism and mineral deposits of the Central Andes (22°–33°S latitude). In: Skinner BJ (ed.), Geology and ore deposits of the central Andes. Soc Economic Geol Special Pub 7:27–59.

Kay SM, Coira BL, Caffe PJ (2008a) Geoquímica, fuentes y evolución del magmatismo neógeno de la Puna Norte. In: Coira B, Zappettini, E (eds), Geología Recursos Naturales Jujuy, Relatorío XVII Congreso Geol Argentino, Asoc Geol Argentina: 322–334

Kay SM, Coira BL, Mpodozis C (2008b) Field trip guide to the Neogene to Recent evolution of the Puna plateau and southern Central Volcanic Zone. In: Kay SM, Ramos VA (eds) Field trip Guides to the Backbone of the America in the Southern and Central Andes. Geol Soc Am Field Guide Series 13:117–181

Kraemer B, Adelmann D, Alten M, Schnurr W, Erpenstein K, Kiefer E, van den Bogaard P, Gorler K (1999) Incorporation of the Paleogene foreland into the Neogene Puna plateau: the Salar de Antofalla area, NW Argentina. J South Am Earth Sci 12:157–182

Lindsay JM, Schmitt AK, Trumbull RB, de Silva SL, Siebel W, Emmermann R (2001) Magmatic evolution of the La Pacana caldera system, Central Andes, Chile: compositional variation of two cogenetic, large-volume felsic ignimbrites. J Petrol 42:459–486

Masuda A, Nakamura N, Tanaka T (1973) Fine structure of mutually normalized rare-earth patterns of chondrites. Geochim Cosmochim Acta 37:239–248

McGlashan N, Brown LD, Kay SM (2008) Crustal thicknesses in the Central Andes from teleseismically recorded depth phase precursors. Geophys J Int 175:1013–1022

Münker C, Wörner G, Yogodzinski G, Churikova T (2004) Behaviour of high field strength elements in subduction zones: constraints from Kamchatka-Aleutian arc lavas. Earth Planet Sci Lett 224:275–293

Ren M (2004) Partitioning of Sr, Ba, Rb, Y and LREE between alkali feldspar and peraluminous silicic magmas. Am Mineralogist 89:1290–1304

Renne PR, Swisher CC, Deino AL, Karner DB, Owens TL, DePaolo DJ (1998) Intercalibration of standards, absolute ages and uncertainties in $^{40}Ar/^{39}Ar$ dating. Chem Geol 145:117–152

Risse A, Trumbull RB, Coira B, Kay SM, van den Bogaard P (2008) $^{40}Ar/^{39}Ar$ geochronology of basaltic volcanism in the back-arc region of the southern Puna plateau, Argentina. J South Am Earth Sci 26:1–15

Rogers G, Hawkesworth CJ (1989) A geochemical traverse across the north Chilean Andes: evidence for crustal generation from the mantle wedge. Earth Planetary Sci Lett 91:271–285

Rudnick RL, Fountain D (1995) Nature and composition of the continental crust: a lower crustal perspective. Rev Geophys 33:267–309

Schmitt A (2002) Gas-saturated crystallization and degassing in large-volume, crystal-rich dacite magmas from the Altiplano-Puna, northern Chile. J Geophys Res 106(30):651-30–578

Schmidt MW, Dardon A, Chazot G, Vannucci R (2004) The dependence of Nb and Ta rutile–melt partitioning on melt composition and Nb/Ta fractionation during subduction processes. Earth Planetary Sci Lett 226:415–432

Schnurr WB, Trumbull RB, Clavero J, Hahne K, Siebel W, Gardeweg M (2007) Twenty-five million years of silicic volcanism in the

southern Central Volcanic Zone of the Andes: Geochemistry and magma genesis of ignimbrites from 25° to 27°S, 67° to 72°W. J Volcan Geoth Res 266:27–46

Sisson TW, Ratajeski K, Hankins WB, Glazner AF (2002) Voluminous granitic magmas from common basaltic sources. Contrib Mineral Petrol 148:635–661

Soler MM, Caffe P, Coira B, Onoe AT, Kay SM (2007) Geology of the Vilama caldera: correlations and a new interpretation of a large scale explosive event in the Central Andean plateau during the Upper Miocene. J Volcanol Geoth Res 164:27–53

Sparks RSJ, Francis PW, Hamer RD, Pankhurst RJ, O'Callaghan LL, Thorpe RS, Page RS (1985) Ignimbrites of the Cerro Galán Caldera, NW Argentina. J Volcan Geoth Res 24:205–248

Steiger RH, Jaeger E (1977) Subcommission on geochronology; convention on the use of decay constants in geo- and cosmo-chronology. Earth Planetary Sci Lett 36:359–362

Stormer JC, Whiney JA (1985) Two feldspar and iron-titanium oxide equilibria in silicic magmas and the depth of origin of large volume ash-flow tuffs. Am Mineral 70:62–64

Sun S-s, McDonough WF (1989) Chemical and isotopic systematics of oceanic basalts; implications for mantle composition and processes. In: Saunders AD, Norry MJ (eds), Magmatism in the Ocean Basins. Geol Soc Special Pub 42:313–345

Watson EB, Harrison TM (1983) Zircon saturation revisited: temperature and composition effects in a variety of crustal magma types. Earth Planet Sci Lett 64:295–304

Wen S, Nekvasil H (1994) SOLVCALC: an interactive graphics program package for calculating the ternary feldspar solvus and for two-feldspar geothermometry. Comput Geosci 20:1025–1040

White SM, Crisp JA, Spera FA (2006) Long-term volumetric eruption rates and magma budgets. Geochemistry, Geophysics, Geosystems 7:doi:10.1029/2005GC001002.

Wiechert U, Fiebig J, Przybilla R, Xiao Y, Hoefs J (2002) Excimer laser isotope-ratio-monitoring mass spectrometry for in situ oxygen isotope analysis. Chem Geol 182:179–194

Wölbern I, Heit B, Yuan X, Asch G, Kind R (2009) Receiver function images from the Moho and the slab below the Altiplano and Puna plateaus in the Central Andes. Geophysical J Int 177:296–308

Wyllie PJ, Huang WL, Stern CR, Maaloe S (1976) Granitic magmas —possible and impossible sources, water contents and crystallization sequences. Canadian J Earth Sci 13:1007–1019

Yuan X, Sobolev SV, Kind R, Oncken O, Bock G, Asch G et al (2000) Subduction and collision processes in the central Andes constrained by converted seismic phases. Nature 408:958–961

Zellmer GF, Clavero JE (2006) Using trace element correlation patterns to decipher a sanidine crystal growth chronology: an example from Taapaca volcano, Central Andes. J Volcanol Geoth Res 156:291–301